



VCU

Virginia Commonwealth University
VCU Scholars Compass

Theses and Dissertations

Graduate School

2012

Segmentation and Fracture Detection in CT Images for Traumatic Pelvic Injuries

Jie Wu

Virginia Commonwealth University

Follow this and additional works at: <https://scholarscompass.vcu.edu/etd>



Part of the [Engineering Commons](#)

© The Author

Downloaded from

<https://scholarscompass.vcu.edu/etd/366>

This Dissertation is brought to you for free and open access by the Graduate School at VCU Scholars Compass. It has been accepted for inclusion in Theses and Dissertations by an authorized administrator of VCU Scholars Compass. For more information, please contact libcompass@vcu.edu.

School of Engineering
Virginia Commonwealth University

This is to certify that the dissertation prepared by Jie Wu entitled Segmentation and Fracture Detection in CT Images for Traumatic Pelvic Injuries has been approved by her committee as satisfactory completion of the dissertation requirement for the degree of Doctor of Philosophy

Kayvan Najarian, Ph.D., Committee Chair, Department of Computer Science

Rosalyn H Hargraves, Ph.D., Department of Electrical and Computer Engineering, School of Engineering

Meng Yu, Ph.D., Department of Computer Science, School of Engineering

David Primeaux, Ph.D., Department of Computer Science, School of Engineering

Kevin R. Ward, M.D., Department of Emergency Medicine, School of Medicine

Todd Wittman, Ph.D., Department of Mathematics and Applied Mathematics, College of Humanities and Sciences

Date

© Jie Wu, 2012

All Rights Reserved

SEGMENTATION AND FRACTURE DETECTION IN CT IMAGES FOR
TRAUMATIC PELVIC INJURIES

A dissertation submitted in partial fulfillment of the requirements for the degree of
Doctor of Philosophy at Virginia Commonwealth University.

by

JIE WU

B.S., Northeastern University (Shenyang, China), 2006

M.S., Northeastern University (Shenyang, China), 2008

M.S., Virginia Commonwealth University (Richmond, USA), 2011

Director: KAYVAN NAJARIAN
ASSOCIATE PROFESSOR, DEPARTMENT OF COMPUTER SCIENCE

Virginia Commonwealth University
Richmond, Virginia
April, 2012

Acknowledgement

I would like to express my deepest gratitude to my advisor, Dr. Kayvan Najarian, for his guidance and support in my research project. He provided me with a valuable chance to do research in this lab. Without his help and encouragement, this research work could not have been completed. I am grateful to all my committee members for their comments and feedback on my work. They are: Dr. Rosalyn Hobson, Dr. Yu Meng and Dr. David Primeaux in the VCU School of Engineering; Dr. Kevin Ward in the MCV Department of Emergency Medicine; Dr. Todd Wittman in the Department of Mathematics and Applied Mathematics. In particular, I greatly appreciate the time Dr. Rosalyn Hobson spent in reviewing and revising my papers. She provided me valuable feedback and suggestions, as well as helped me a lot during the Ph.D. study. I also thank Dr. Charles Cockrell and Dr. Tang Yang in the MCV Department of Radiology, who gave me very helpful suggestions for improving my research work. Dr. Charles Cockrell kept providing the data for this project from the earliest stage of my work. The advice from all of them was very useful and gave me a new perspective on my research. I also thank Pavani Davuluri, who offered me advice and support while we worked on this project.

I thank all the members in Biomedical Signal and Image Processing Lab of Computer Science Department, who have made the life a lot of fun. Most of all, I thank

my incredible family, especially my parents, and my friends, for their persistent support on my Ph.D. study and my life in the United States.

This material is based upon work supported by the National Science Foundation under Grant No. IIS0758410. The dataset used for this project is provided by Virginia Commonwealth University Medical Center.

Table of Contents

	Page
Acknowledgements.....	ii
List of Tables	viii
List of Figures	ix
Abstract.....	xiii
Novelty and Contribution.....	xvi
 Chapter	
1 Introduction.....	1
1.1 Overview	1
1.2 Problem Statement	1
1.3 Computed Tomography (CT)	4
1.4 Anatomy of Pelvis	5
1.5 Medical Image Segmentation.....	6
1.6 Proposed Method.....	12
2 Methods for Pre-processing and Edge Detection.....	16
2.1 Overview	16
2.2 Pre-processing	17
2.3 Image Enhancement	19
2.4 Edge Detection	23
2.5 Summary	26

3	Methods for Shape Matching and Best Template Detection	27
3.1	Overview	27
3.2	Shape Matching	27
3.3	Summary	32
4	Methods for Registered Active Shape Model	33
4.1	Overview	33
4.2	Active Shape Model.....	34
4.3	Image Registration	35
4.4	Registered Active Shape Model (RASM)	39
4.5	Initialization for RASM.....	41
4.6	3D pelvic bone visualization	45
4.7	Summary	45
5	Fracture Detection and Displacement Measurement	47
5.1	Overview	47
5.2	Methodology for fracture detection.....	47
5.2.1	Adaptive window creation.....	48
5.2.2	The 2-D stationary wavelet transform.....	50
5.2.3	Masking	53
5.2.4	Boundary tracing	54
5.3	Quantitative displacement measure.....	55

5.4	Summary	56
6	Results of Image Processing	57
6.1	Overview	57
6.2	Dataset	57
6.3	Results for segmentation	58
6.3.1	Results for eliminating surrounding artifacts and extracting the pelvic region.....	58
6.3.2	Results for image enhancement.....	60
6.3.3	Results for edge detection	62
6.3.4	Results for matching a template to the analyzed slice.....	64
6.3.5	Results for homogeneity feature extraction.....	66
6.3.6	Results for image segmentation	68
6.3.7	Evaluation measures.....	72
6.3.8	Compared results with Snake.....	75
6.3.9	Consideration during Training.....	77
6.4	Results for fracture detection	85
6.5	Results of 3D pelvic bone structure modeling.....	90
6.6	Summary and discussion	93
7	Conclusion and Future Work	96
7.1	Overview	96
7.2	Conclusions	96

7.2	Future Work	97
7.2	Summary	97
Bibliography		98

List of Tables

	Page
Table 6.1: Evaluation of the matching results using Shape Matching and Correlation Coefficients.....	64
Table 6.2: Performance of three training models for the first testing data.....	80
Table 6.3: Performance of three training models for the second testing data.....	81
Table 6.4: Performance of three training models for the third testing data.....	82
Table 6.5: Performance of three training models for the fourth testing data.....	83
Table 6.6: Performance of pelvic bone fracture detection.....	88
Table 6.7: Performance of pelvic bone fracture detection.....	88

List of Figures

	Page
Figure 1.1: CT imaging device	5
Figure 1.2: Sample pelvic CT image	6
Figure 1.3: A brief overview of pelvic structures	7
Figure 1.4: Schematic diagram of pelvic bone segmentation	13
Figure 1.5: The framework of the proposed decision-making system.....	15
Figure 2.1: Setup for pre-processing process.....	16
Figure 2.2: Diagram for the pre-processing (Abdominal region extraction) step.....	18
Figure 2.3: Example results for Abdominal Region Extraction	19
Figure 2.4: Image enhancement via contrast stretching.....	20
Figure 2.5: Contrast enhancement processing	21
Figure 2.6: Example results for the image enhancement	22
Figure 2.7: Schematic diagram of preliminary pelvic bone segmentation	24
Figure 2.8: Spurs Removal	25
Figure 2.9: Example results for the edge detection.....	25
Figure 3.1: Shape matching process	29
Figure 3.2: Diagram of the log-polar bins used to compute the shape context	31
Figure 4.1: Image registration algorithm	38
Figure 4.2: Example results for Homogeneity extraction.....	38
Figure 4.3: Example result of image registration.....	39

Figure 4.4: RASM Algorithm	40
Figure 4.5: Comparison of standard shape model and registered shape model.....	41
Figure 4.6: Proposed initialization process for RASM.....	44
Figure 4.7: Diagram of segmentation using RASM and initialization process	44
Figure 5.1: Schematic diagram of pelvic bone fracture detection	48
Figure 5.2: Example windows around the boundary of pelvic bone, positioned according to landmarks.....	50
Figure 5.3: Decomposition steps of 2-D SWT.....	53
Figure 5.4: Sample results of fracture detection	55
Figure 5.5: Displacement calculation	56
Figure 6.1: Sample results for extracting the pelvic region from the raw CT Image	59
Figure 6.2: Example results for image enhancement.....	61
Figure 6.3: Example results for preprocessing and edge detection	63
Figure 6.4: Example results of shape matching	65
Figure 6.5: Example result of best shape matching Template	66
Figure 6.6: Example results for homogeneity extraction.....	68
Figure 6.7: Example of pelvic bone segmentation results via RASM.....	70
Figure 6.8: Example results of pelvic bone segmentation via Standard ASM without initialization.....	71
Figure 6.9: Example results of pelvic bone segmentation via Standard ASM with manual initialization.....	71

Figure 6.10: Inaccurate segmentation result.....	71
Figure 6.11: Segmentation accuracy results using proposed method of different pelvic bone structures	74
Figure 6.12: Segmentation accuracy including both Good and Acceptable results of different pelvic bones using proposed method, Standard ASM with manual initialization and Standard ASM without initialization.	75
Figure 6.13: Compared results of pelvic bone segmentation via RASM and Snake methods.....	77
Figure 6.14: Results of pelvic ilium bone segmentation using three different training models for a testing subject.....	83
Figure 6.15: Results of pelvic ilium bone segmentation using three different training models for a testing subject.....	83
Figure 6.16: Results of pelvic ilium bone segmentation using three different training models for a testing subject.....	84
Figure 6.17: Results of pelvic ilium bone segmentation using three different training models for the second testing subject.....	84
Figure 6.18: Results of pelvic femur bone segmentation using three different training models for a testing subject.....	84
Figure 6.19: Results of pelvic femur bone segmentation using three different training models for a testing subject.....	84
Figure 6.20: Results of pelvic pubic bone segmentation using three different training models for a testing subject.....	85
Figure 6.21: Results of pelvic pubic bone segmentation using three different training models for a testing subject.....	85
Figure 6.22: Example of a detected broken boundary of pelvic bone, which may indicate a fracture	86

Figure 6.23: Example of a detected non-broken boundary of pelvic bone, which may indicate no fracture	86
Figure 6.24: Example of a detected broken boundary of pelvic bone, which may indicate three fractures	87
Figure 6.25: Example results of inaccurate fracture detection.....	89
Figure 6.26: Example results of 3D pelvic bone structure.....	90

Abstract

SEGMENTATION AND FRACTURE DETECTION IN CT IMAGES FOR TRAUMATIC PELVIC INJURY

By Jie Wu, Ph.D. Candidate

A dissertation submitted in partial fulfillment of the requirements for the degree of Doctor
of Philosophy at Virginia Commonwealth University.

Virginia Commonwealth University, 2012

Major Director: Kayvan Najarian
Associate Professor, Department of Computer Science

In recent decades, more types and quantities of medical data have been collected due to advanced technology. A large number of significant and critical information is contained in these medical data. High efficient and automated computational methods are urgently needed to process and analyze all available medical data in order to provide the physicians with recommendations and predictions on diagnostic decisions and treatment planning.

Traumatic pelvic injury is a severe yet common injury in the United States, often caused by motor vehicle accidents or fall. Information contained in the pelvic Computed Tomography (CT) images is very important for assessing the severity and prognosis of traumatic pelvic injuries. Each pelvic CT scan includes a large number of slices.

Meanwhile, each slice contains a large quantity of data that may not be thoroughly and accurately analyzed via simple visual inspection with the desired accuracy and speed. Hence, a computer-assisted pelvic trauma decision-making system is needed to assist physicians in making accurate diagnostic decisions and determining treatment planning in a short period of time.

Pelvic bone segmentation is a vital step in analyzing pelvic CT images and assisting physicians with diagnostic decisions in traumatic pelvic injuries. In this study, a new hierarchical segmentation algorithm is proposed to automatically extract multiple-level bone structures using a combination of anatomical knowledge and computational techniques. First, morphological operations, image enhancement, and edge detection are performed for preliminary bone segmentation. The proposed algorithm then uses a template-based best shape matching method that provides an entirely automated segmentation process. This is followed by the proposed Registered Active Shape Model (RASM) algorithm that extracts pelvic bone tissues using more robust training models than the Standard ASM algorithm. In addition, a novel hierarchical initialization process for RASM is proposed in order to address the shortcoming of the Standard ASM, i.e. high sensitivity to initialization. Two suitable measures are defined to evaluate the segmentation results: Mean Distance and Mis-segmented Area to quantify the segmentation accuracy. Successful segmentation results indicate effectiveness and robustness of the proposed algorithm. Comparison of segmentation performance is also conducted using both the proposed method and the Snake method. A cross-validation process is designed to

demonstrate the effectiveness of the training models. 3D pelvic bone models are built after pelvic bone structures are segmented from consecutive 2D CT slices.

Automatic and accurate detection of the fractures from segmented bones in traumatic pelvic injuries can help physicians detect the severity of injuries in patients. The extraction of fracture features (such as presence and location of fractures) as well as fracture displacement measurement, are vital for assisting physicians in making faster and more accurate decisions. In this project, after bone segmentation, fracture detection is performed using a hierarchical algorithm based on wavelet transformation, adaptive windowing, boundary tracing and masking. Also, a quantitative measure of fracture severity based on pelvic CT scans is defined and explored. The results are promising, demonstrating that the proposed method not only capable of automatically detecting both major and minor fractures, but also has potentials to be used for clinical applications.

Novelty and Contributions

Medical data contains information that is vital for clinical diagnosis as well as treatment planning. Nowadays, varieties of clinical data are not optimally and comprehensively utilized towards medical decision making. This is because simple human inspection or traditional computational methods are incapable of extracting the hidden patterns contained in the data, which are very important to form recommendations and predictions for both diagnosis and treatment planning. Traumatic Pelvic Injury constitutes a major cause of death in the United States every year. A computer-assisted pelvic trauma decision making system is crucial to assist physicians make accurate and faster diagnostic decisions and treatment planning. Currently however, due to factors such as limited resolution of medical images, variations in bone tissues, complexity of pelvic structures, and significantly different geometrical characteristics of fractures, automatic segmentation of pelvic bone and detection of the bone fractures in CT scan remain as challenging tasks. In addition, the existing decision-making systems for traumatic injuries do not extract and/or consider the features automatically detected from medical images. The focus of this dissertation is on developing a system to extract diagnostic features from pelvic CT images, which incorporate new computational methodologies for automatic bone segmentation and fracture detection. The proposed system has several novel components, including:

- 1) A new segmentation algorithm for multiple pelvic CT scans is proposed, which consist of pre-processing, Shape Matching, and Registered Active Shape Model (RASM). For pre-processing, a hierarchical method to perform preliminary bone

segmentation is proposed that incorporates morphological operations, image enhancement, and edge detection. This method is explained in Chapter 2. Next, the proposed hierarchical segmentation method provides automation partially due to the use of a shape matching algorithm. This method is described in Chapter 3.

- 2) A new image registration algorithm is devised to couple with Active Shape Model to create shape models. This registration method applies enhanced homogeneity feature extraction, correlation coefficient calculation for similarity measure, affine transformation, and Powell algorithm application. This algorithm is explained in Chapter 4.3.
- 3) A new family of Active Shape Model algorithm – Registered Active Shape Model (RASM) is proposed in order to create more robust training models. The pelvic bones in each original training image have different sizes, rotation angles and locations. After the pelvic bones in each training image are registered to the corresponding anatomical template, more robust and reliable training models are created for better segmentation performance. The RASM algorithm is explained in Chapter 4.4.
- 4) Based on the designed RASM algorithm, another novel extension of this algorithm is used in this project. A hierarchical initialization algorithm is proposed, to address the main shortcoming of the Standard ASM – high sensitivity to initialization. If the shape model is not accurately placed, the Standard ASM method may fail to detect the target object. The proposed initialization process is composed of image registration, extracted bone features as well as prior edge detection results to

sequentially and automatically place the training models on each individual object.

This is explained in Chapter 4.5.

- 5) A training model validation process is designed to demonstrate that the selection of training data has a very small effect on the segmentation outcome. The validation process also shows that generated training models are reliable and effective. This is explained in Chapter 6.3.9.
- 6) In this dissertation, an automated algorithm is designed to detect the fractures in the pelvic bone by analyzing the segmented images and detecting discontinuity. This method is achieved by creating a series of adaptive windows based on the boundaries extracted from the segmentation process performed by RASM. This algorithm sequentially tests the bone boundary of each slice for contour discontinuities which may indicate fracture. This technique is explained in Chapter 5.
- 7) The methodologies developed by this project can be applied for segmentation as well as detection of bone fracture in other types of medical images captured from other parts of human body. The method can also be used for segmentation of unanimated objects.

CHAPTER 1 Introduction

1.1 Overview

This chapter explains the importance and urgent demand of computer-assisted decision-making systems for traumatic injuries, especially for traumatic pelvic injuries. The chapter first provides an overview of Computed Tomography technology and anatomy of the pelvis. Then, a general overview of the relevant previous work in medical image segmentation methods is given. Finally, this chapter concludes with a high-level description of the ideas of the proposed method.

1.2 Problem Statement

Traumatic pelvic injuries are often high energy injuries that constitute a major cause of death in trauma patients. Every year, traumatic pelvic injuries contribute to cases of death and permanent disability. Latest U.S. statistics available from the National Center for Health Statistics shows that more than 40,000 motor vehicle related deaths occurred and more than 20,000 fall deaths occur every year [1]. According to the Centers for Disease Control and Prevention (CDC), trauma injury kills more people between the ages of 1 and 44 than any other disease or illness [2]. On average, 15 U.S. workers die each day from traumatic injuries [3], simultaneously, thousands of U.S. workers visit emergency rooms for treatment of work-related traumatic injuries every day [4]. More than 300 patients with pelvic fractures were seen in less than 3 years at the University of Maryland Shock Trauma Center [5], and Patients with pelvic bone fractures who are present in shock have a mortality of 30-50% [6]. When combined with injuries in other body regions, for

example, the abdomen, the chance of mortality rises even higher, approaching 100% in some cases [6]. Among different types of trauma with a high impact on the lives of Americans, traumatic pelvic injuries, caused mainly by sports, falls and motor vehicle accidents contribute to a large number of mortalities every year [7, 8]. Traumatic pelvic injuries and associated complications, such as severe hemorrhage, multiple organ dysfunction syndrome (MODS), and blood clots traveling to the brain or lungs, result in the mortality rate from 8.6% to 50% [9]. From anatomical aspect, a pelvic fracture can be associated with bleeding, injury to the nerves, and internal organ damage as all of the vital structures run through pelvis. Complications, such as pain and impaired mobility are usually the result of nerve and organ damage associated with the pelvic fracture [10].

Young people, especially those doing sports are at risk for pelvic fracture. Sudden muscle contractions normally occur with these fractures. Elderly people suffer from osteoporosis may get a pelvis fracture during a fall from standing or walking. Usually the structural integrity of the pelvic ring may not damage in these injuries, instead an individual bone may be broken. The main cause of a pelvic fracture is a motor vehicle accident, crush accident or fall from a high place.

For the patients with traumatic pelvic injuries, information contained in pelvic Computed Tomography (CT) images is a very important resource for assessing the severity and prognosis of such injuries. Each pelvic CT scan consists of many slices; a large amount of data contained in each slice may not be thoroughly and accurately analyzed via simple visual observation. In addition, in the field of trauma medicine, caregivers are frequently confronted with situations in which they need to make rapid decisions based on

a massive amount of information. As such, developing a computer-assisted pelvic trauma decision-making system is the goal of this project. Such a system is necessary to assist physicians make accurate diagnostic and decide treatment planning decisions in a short period of time. Although some computer-assisted trauma decision making systems have been developed, but majority of them mainly rely on the similarities between demographics of the patients. The past cases in trauma databases provide the recommendation to get the outcome. Therefore, these recommendations may ignore the important information regarding the injury and not be accurate and reliable enough in making diagnostic decisions [48]. In our project, the system consider the wealth of information contained in medical data, conduct bone segmentation and fracture detection, build 3D pelvic bone models as well, which are highly important for assessing the injury severity.

Automatic fracture detection from segmented bones in traumatic pelvic injuries can help physicians process and analyze the pelvic CT images and detect the severity of injuries in patients. If the fracture is due to a high-energy injury, there is often a large amount of bleeding, which can lead to shock. Depending on the direction and degree of force, the injuries can be very severe and become life-threatening. As a result, such injuries may require immediate and accurate decision-making. Hence, extraction of fracture features, such as presence and location of the fracture, as well as bone displacement measurement, is very important in order to assist physicians in making fast and accurate decisions. However, fracture detection in pelvic bones is very challenging due to the limited resolution of the original CT images and the complexity of pelvic structures and

their possible fractures. In addition, CT images are also susceptible to noise, partial volume effects, and in-homogeneities. These make fracture detection more challenging and time-consuming. Fracture detection in pelvic CT images is still an under-explored field. To date, there are very few direct fracture detection studies focused on pelvic CT images. M. H. Moghari et al. [71] utilized a global registration for multi-fragment fracture fixation in femur bones. However, the method suffers from initial alignment errors, and the dataset only includes femur bones, generated randomly from 3-D data points. M. H. Moghari et al. [72] applied global registration of multiple bone fragments using Statistical Atlas Models, but due to the limited number of bone models, this work is not enough to capture all variations of the femur bone. S. Winkelbach et al. [73] used Pose Estimation of cylindrical fragments for bone fracture reduction; though this method is not fully automatic. There is also related work in X-ray images [74-76]. Douglas TS et al. [74] focused on early detection of fractures with low-dose digital x-ray images in a pediatric trauma unit, M. A. Png et al. [75] determined the presence of femoral fracture by measuring the neck shaft angle of the femur; however, these are indirect detection methods. V. L. F. Lum [76] used three texture features based combined classifiers to detect radius and femur fractures; however, this method suffered from the imbalanced dataset. When applying those methods of detecting fracture in X-ray images, it is hard to achieve desirable results in CT images because of their different characteristics, intensities and resolutions.

1.3 Computed Tomography(CT)

Computed tomography (CT) is a medical imaging method employing tomography created by computer processing [13]. CT scanning combines special x-ray equipment with

sophisticated computers to produce multiple images or pictures of the inside of the body, which appear as “slices” of tissues [14].

CT images are composed of a certain number of pixels associated with the attenuation values of the tissue located at the corresponding points. Different sizes and numbers of pixels in CT images can be obtained from different CT devices. The smaller the size of pixels, the higher the spatial resolution of the image is. In CT images, the shadows are the regions with low absorption of X-ray, which are the low-density areas, such as the lungs while the white regions indicate high absorption of X-ray, which are high-density areas, such as bone. CT value is the numeric measure that describes the density. The unit is Hu (Hounsfield Unit). For example, the CT value of water is 0Hu. Different tissues in the human body have different densities; the CT values range from -1000 Hu to +1000 Hu. Figure 1.1 is an example of CT imaging devices. Figure 1.2 shows a sample of pelvic CT image.



Figure 1.1: CT imaging device (North Dallas Radiation Oncology Center)

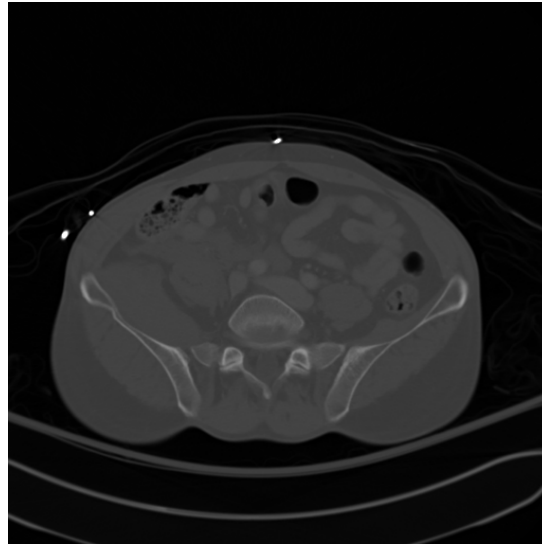


Figure 1.2: Sample pelvic CT image.

1.4 Anatomy of Pelvis

The pelvis is the part of the trunk inferioposterior to the abdomen in the transition area between the trunk (torso) and the lower limbs [15]. The main function of the pelvis is to bear the weight of the upper body when sitting or standing. Many digestive and reproductive organs are located within the pelvis. There are also many large nerves and blood vessels passing through the pelvis and extending to the legs.

In adults, the pelvis mainly consists of two hip bones, one is on the right side of the body and the other is on the left. These two hip bones consist of three separate bones: the ilium, ischium and pubis. Along with the hip bones, the sacrum is also the component of the pelvis, which is located in the upper-middle portion. This bone connects the spine and the pelvis. Figure 1.3 shows the pelvis structure.

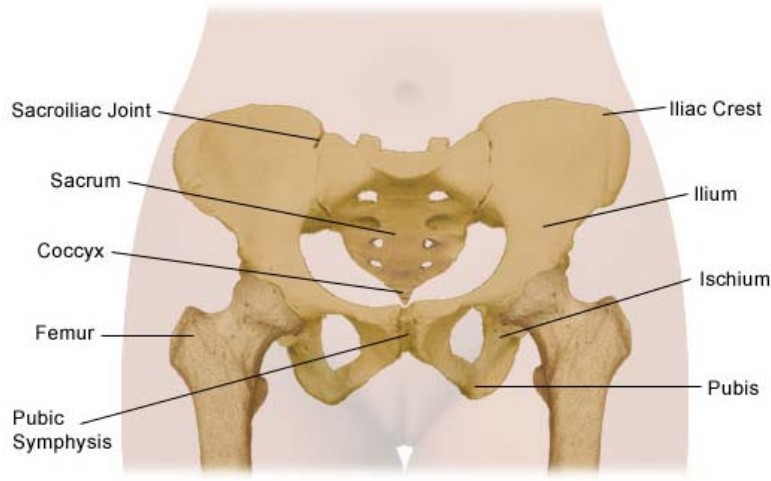


Figure 1.3: A brief overview of pelvic structures. (Rush University Medical Center, Chicago, Illinois)

1.5 Medical Image Segmentation

Segmentation is the process of partitioning a digital image into multiple segments (sets of pixels), which collectively cover the entire image. The goal of segmentation is to change the representation of an image to analyze it in a more meaningful and easier manner [16]. The mathematical definition of image segmentation is given as follows:

If the domain of the image is given by I , the segmentation problem is to determine the sets $S_m \subset I$, whose union is the entire image I . Thus, the sets which make up a segmentation satisfy

$$I = \bigcup_{m=1}^M S_m \quad (1.1)$$

where $S_m \cap S_n = \emptyset$ for $m \neq n$, and each S_m is connected. In image processing field, pixel connectivity is the way in which two or three dimensional images related to their neighbors. Eight-connection is defined as follows.

8-connected pixels are neighbors to every pixel that reaches one of their edges or corners. These pixels are connected horizontally, vertically, and diagonally. Each pixel with coordinates $(x \pm 1, y \mp 1)$ or $(x \pm 1, y \pm 1)$ or $(x \pm 1, y)$ or $(x, y \pm 1)$ is connected to the pixel at (x, y) . A path within the image is defined as the sequence of the connected pixels.

Image segmentation algorithms play a significant role in many biomedical imaging applications, such as quantification of tissue volumes [17], diagnosis [18], localization of pathology [19], study of anatomical structure [20], treatment planning [21], partial volume correction of functional imaging data [22], and computer integrated surgery [23,24]. Currently, there is no general image segmentation algorithm which yields satisfied results for every medical image. Different clinical applications, different modalities of images, and other factors, such as different types of noise, require customized segmentation algorithms. For example, the segmentation of brain tissue differs from the segmentation of the pelvis or abdomen. General imaging artifacts, including noise, motion and other factors also influence the performance of segmentation methods. Therefore, it is difficult to select an appropriate approach for a specific segmentation issue.

Medical segmentation is one of the vibrant research topics in the field of medical image processing. Several advanced methods have been introduced in recent years for the segmentation of medical images [2]. Currently, the existing image segmentation methods can be divided into the following categories: (1) thresholding approaches; (2) region growing approaches; (3) classifiers; (4) clustering approaches; (5) Markov random field models; (6) artificial neural networks; (7) deformable models, and (8) atlas guided approaches. Thresholding, classifier, clustering, and Markov random field approaches can

be considered as pixel classification methods. In recent years, new variations of these segmentation methods have been proposed [25-28]. A brief description of these existing image segmentation methods is given as follows:

- Thresholding

Thresholding technique segments an image by creating a binary partitioning of the image intensities [29]. An intensity value, called the “threshold”, is determined to separate the desired classes. The segmentation process is then achieved by grouping all pixels with intensity greater than the threshold into one class and all other pixels into another class. The technique is effective for the images that contain different structures with distinct intensities. It is often applied as the initial step in a sequence of processing operations. The first drawback of thresholding technique is that it cannot be directly applied to multi-channel images. Secondly, it does not take into account the spatial characteristics of an image. Hence, often it is impossible to characterize the pixels in the segmented region with a single threshold value.

- Region growing

Region growing is a technique for extracting a connected region of an image based on a predefined criterion [30, 39]. In this method, an initial set of seeds is chosen and new points are added to the region if they meet a certain similarity criterion. Region growing is used for image processing applications, such as delineation of simple structures like tumors and lesions. However, this technique is sensitive to the choice of the initial seed. It also requires manual interaction to form the seed points. Region growing can also be sensitive to noise, causing extracted regions to have holes resulting to disconnected regions.

- Clustering

Clustering algorithms are also referred to as unsupervised methods [31, 40]. In cluster segmentation, a set of clusters are created to segment the target image into regions. Some of the commonly used clustering techniques are K-means [32], the fuzzy c-mean algorithm [33], and the expectation-maximization algorithm [34, 35]. Clustering algorithms do not directly incorporate spatial modeling and can be sensitive to noise and intensity in homogeneities. Also, calculation of inter- and intra- cluster distances is computationally expensive when the clusters have a large number of pixels.

- Classifiers

Classifier methods seek to partition a feature space derived from the image using data with known labels. Classifiers are supervised methods as they require a set of training data which have been manually segmented. The training set is used as references for automatically segmenting the new data. Nearest-neighbor classifier [45], k-nearest-neighbor classifier [46], and maximum likelihood [47] are commonly used classification methods. One of the disadvantages of such classifiers is that they do not perform any spatial modeling. Another disadvantage is the requirement of manual interaction for obtaining the training data, which is time consuming.

- Markov random field models

Markov random field models (MKFS) is a statistical model which can be used for segmentation. MRFs are often incorporated into clustering segmentation algorithms such as K-means algorithm under a Bayesian prior model [36]. MRF models require proper

selection of the parameters controlling the strength of spatial interactions. Also, they usually require computationally intensive algorithms.

- Artificial neural networks

Artificial neural networks (ANNS) are massively parallel networks of processing nodes which can simulate biological learning. ANN represents a paradigm for machine learning and can be used in a variety of image segmentation techniques. The widest use of these methods is that ANN is treated as a classifier [37, 38], in which the weights of the ANN are using the training data, and the ANN is then used to segment the new data. The processing of ANN is usually simulated in a standard computer, compromising the potential computational advantages of ANN. Some types of ANNs can also be used as clustering methods for segmentation.

- Deformable models

Deformable models motivated by the physics of the problems are model-based techniques for marking region boundaries using closed curves or surfaces. In this approach, an initial contour is desired boundary first should be put near the desired boundary and then through an iterative relaxation process the position of the contour is improved. The disadvantage is that these deformable models methods require manual interaction to place an initial model and to choose appropriate parameters. A review of deformable models in medical image processing can be found in [41].

- Atlas-guided approaches

Atlas-guided methods are powerful tools for medical image segmentation that apply a standard atlas or template to guide segmentation. The atlas or template is generated

based on the previously known anatomical information. The atlas is then used as the reference frame for segmenting new images. The standard atlas-guided approach usually treats segmentation as a registration problem [42]. However, accurate segmentation of complex structures is difficult due to anatomical variability across individuals.

- Other segmentation approaches

There are also some other, often hybrid approaches, for image segmentation. For example, model-fitting is a segmentation method that fits a simple geometric shape such as parabola to the features in an image [43]. The difficulty of model-fitting is that the features in images must be extracted before the fitting can take place. Watershed algorithm segments images into homogeneous regions [44] using the concepts from mathematical morphology. The main shortcoming of watershed algorithm is that it suffers from over-segmentation, which occurs when the image is segmented into unnecessary regions.

1.6 Proposed Method

The first step in fracture detection is bone segmentation, which helps extract the bones from the CT images. Bone segmentation is very important for detecting the fractures in pelvic bones. Bone tissue segmentation by automated CT image processing can significantly reduce the time needed to examine medical images and to improve the accuracy of medical decision-making. However, automatic bone tissue segmentation from each CT image is very challenging due to the complexity of pelvic structures, and variation in bone structure from person to person. In addition, CT images are susceptible to noise, partial volume effects, and in-homogeneities. These make the bone segmentation more

challenging and time-consuming.

In this project, a new hierarchical segmentation algorithm in multi-level pelvic CT scans is developed which can segment the pelvic bones from CT images automatically and accurately, as illustrated in Figure 1.4. The proposed method consists of four parts: preprocessing, edge detection, the best matching template detection and Registered Active Shape Model (RASM) with automatic initialization.

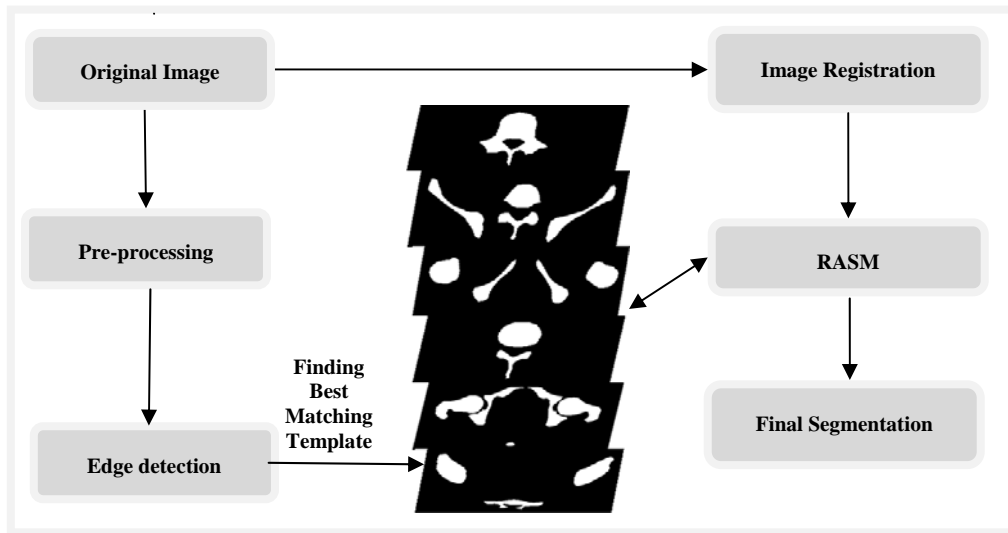


Figure 1.4: Schematic diagram of pelvic bone segmentation

As shown in Figure 1.4, the first step of segmentation is pre-processing. A multi-stage pre-processing technique is introduced, which includes surrounding artifacts filtering, morphological operations, and image enhancement. This step first removes the surrounding artifacts present in the original image, such as CT table, cables, hands, and lower extremities. High frequency speckle noise is also removed from the images using a median filter. Next, the image is enhanced to emphasize the features of interest – for example, the pelvic bone is enhanced to higher intensity while less emphasis is placed on

soft tissues and other organs. Once image enhancement is conducted using brightness contrast stretching, a series of steps are applied for preliminary bone tissue segmentation, including the Canny edge detection technique to detect the edges of bone tissue, morphological operations to remove spurious edges and sub-edge connections and removal. The obtained preliminary segmented results are then used for detecting the best matching template. This process is performed by a template-based best shape matching algorithm [61] to design the segmentation process entirely automatically. For this technique, 100 bone templates are created through manual selection from the Visible Human Project dataset [64], and these templates are compared to each CT slice in order to determine the best matched template, which allows the corresponding training shape models of each best matched template to be applied to the detected edge for bone segmentation. The final bone segmentation is conducted using the proposed Registered Active Shape Model (RASM), to extract pelvic bone tissues using more robust training models than the Standard ASM algorithm. In addition, a novel hierarchical initialization process for RASM is proposed in order to address the shortcoming of initialization to the Standard ASM that it is highly sensitive to the choice of initial points.

After pelvic bones are extracted from 2D CT images, they are used to build the 3D pelvic bone models via the isosurface method. In order to quantify the segmentation accuracy, two suitable measures are defined to evaluate the segmentation results: Mean Distance and Mis-segmented Area. In order to test the reliability of the performance of training models, a cross-validation process is designed to test how much segmentation can be affected by variation in training sets.

Fracture detection is conducted after bone segmentation. In this project, a new hierarchical methodology consisting of a series of computational steps such as adaptive window creation, 2-D SWT application, masking, and boundary tracing is proposed. The ultimate goal of image segmentation and fracture detection is to generate recommendations for decision-making and treatment planning in traumatic pelvic injuries. An overall schematic diagram of high-level description for the decision-making system is illustrated in Figure 1.5.

The rest of this dissertation is organized as follows. Proposed methods for bone segmentation and fracture detection as well as the results are presented in Chapters 2, 3, 4, 5. Chapter 2 gives the methodology for preliminary bone segmentation, including pre-processing and edge detection. Chapter 3 presents the methods for Shape Matching and best template detection. In Chapter 4, the RASM algorithm and initialization process are presented. Chapter 5 explains the hierarchical method for fracture detection. Chapter 6 concludes the dissertation and lists the future work.

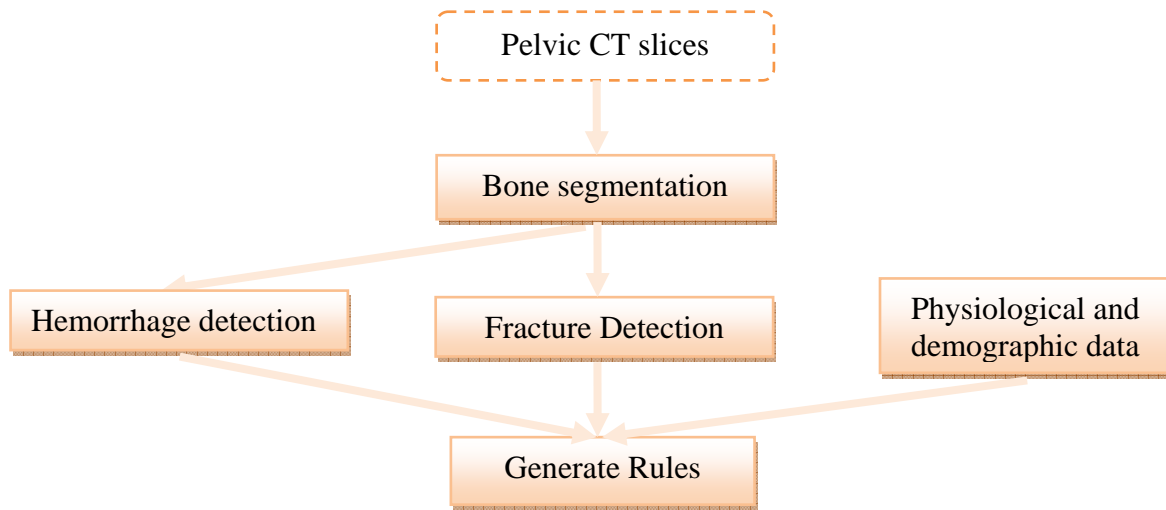


Figure 1.5: The framework of the proposed decision-making system.

CHAPTER 2 Methods for Pre-processing and Edge Detection

2.1 Overview

This chapter presents the methodology for preliminary bone segmentation. A complete schematic diagram for the initial segmentation process is shown in Figure 2.1. The initial segmentation process consists of a series of steps. The preprocessing algorithm for removing surrounding artifacts is given. The chapter proceeds by describing the methods for enhancing the brightness contrast of bone tissues in the original pelvic images. The next section explains the approaches for edge detection. Example results for each subsection are given throughout the chapter.

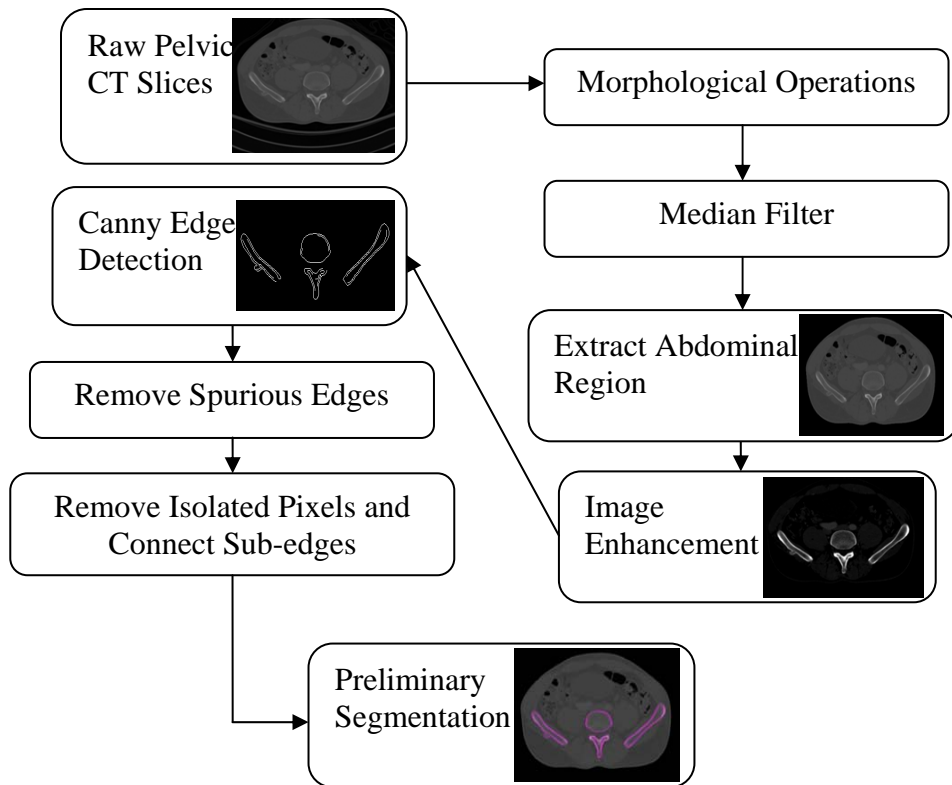


Figure 2.1: An overview of preliminary segmentation process

2.2 Pre-processing

The main purpose of the pre-processing step is to separate the abdomen part as the main subject from the original pelvic CT images. There exist different surrounding artifacts in the original image, e.g. CT table, cables, hands, and lower extremities. Morphological operations are performed in the original image to separate different regions and to select the region with the largest area. Median filter is also applied to remove high frequency speckle noise. Diagram of the pre-processing steps is shown in Figure 2.2. The detail of extracting the abdomen part is laid out as follows:

- Step01: In order to extract the abdominal region, a binary image is created based on the original image. A specified intensity value is set as the threshold. The pixels whose intensity values higher than this threshold are set to 1, and the pixels whose intensity values are less or equal to this threshold are set to 0. The abdominal region and some of the surrounding artifacts have a higher gray level value than the background. Consequently, the abdominal region and some of the artifacts are well separated from the background.
- Step02: Morphological operations are conducted on the binary image. This step is designed to separate different objects in the extracted image. The pelvic region and some artifacts may be connected together in the extracted image; morphological operations are applied to make them disconnected and separated.
- Step03: The region with the largest area – the abdomen is then selected. In this step, first the features of different regions, such as the area and centroid are calculated. Then, the region with the largest area is separated and selected.

- Step04: A mask is created with the same size of the identified region in step 3. This allows additional artifacts to be removed.
- Step05: After the abdomen region is selected, median filter is applied in order to remove the existing high frequency speckle noise in the image. This step is vital to eliminate the noise as the noise can affect features of the structures of interest and degrade the overall quality of the image. Median filters are linear and are described using a mask in space. Median filters reduce noise without destroying the edges. By using median filter, the grey-level of each pixel is replaced by the median of the grey levels in the mask. What makes median filters differ from lowpass filter is the use of “median” as opposed to “average”. Example results are shown in Figure 2.3. The original images are processed based on the steps stated above.

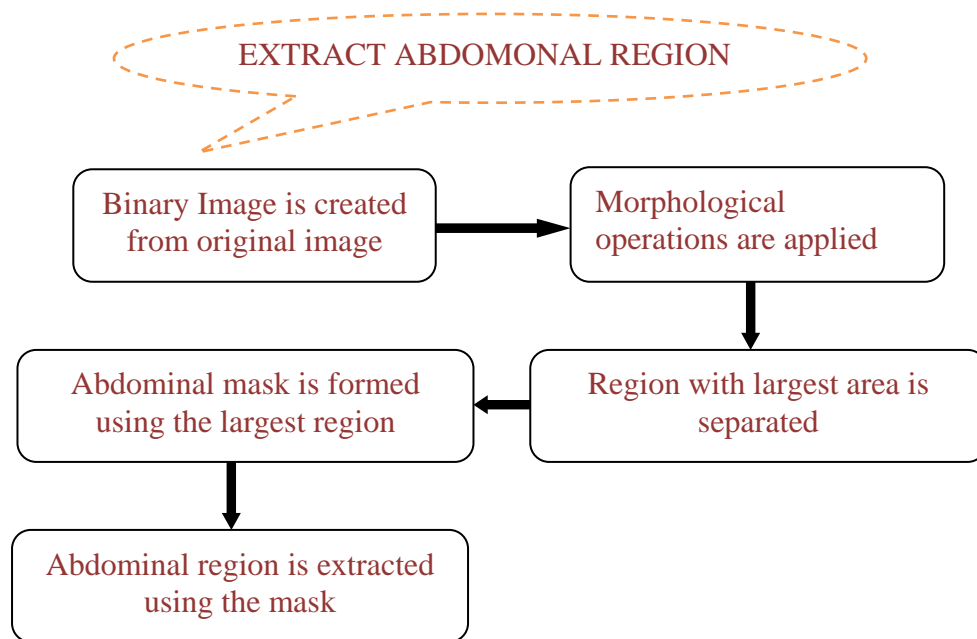
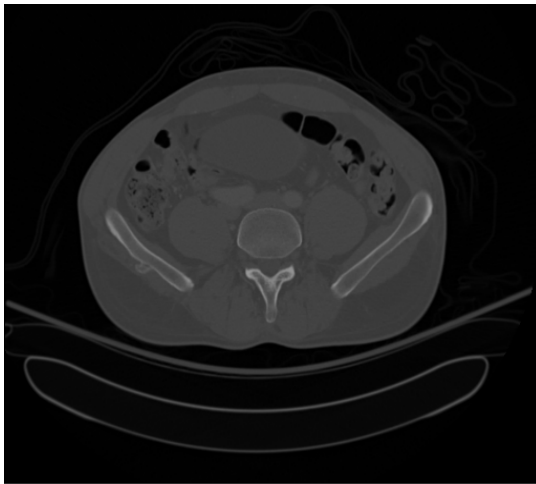


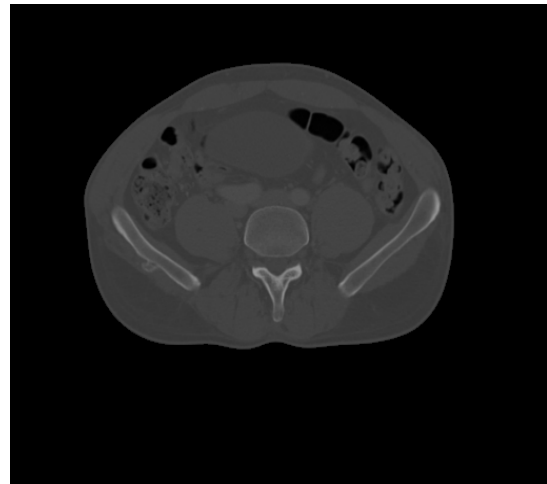
Figure 2.2: Diagram for the pre-processing (Abdominal region extraction) step.

2.3 Image Enhancement

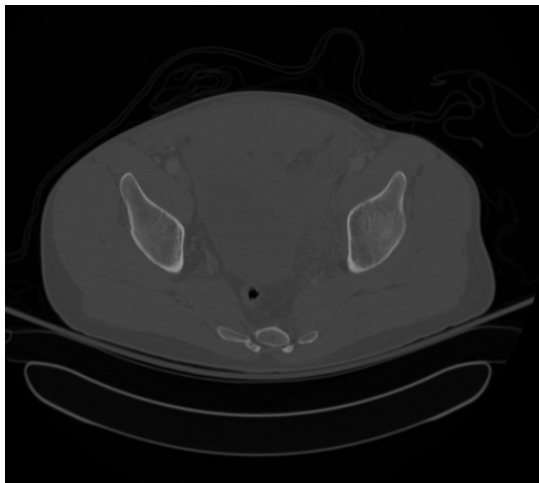
Image enhancement is an image processing task to improve the interpretability or perception of information in images for viewers [49]. Image enhancement is involved in our algorithm to emphasize the features of interest – the pelvic region, while simultaneously put less emphasis on soft tissues and other organs. This ensures that the original image quality is improved with “better” information reflected about pelvic bones.



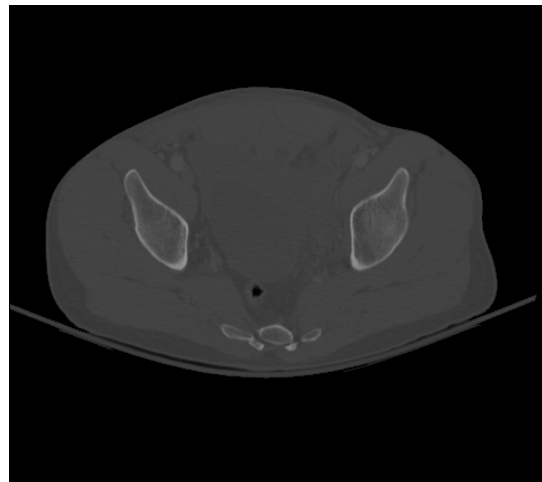
(a) Original pelvic CT image example A



(b) Extracted abdominal region example B



(c) Original pelvic CT image example B



(d) Extracted abdominal region example B

Figure 2.3: Example results for Abdominal Region Extraction.

The techniques for image enhancement are classified to two types: the techniques in spatial domain and the techniques in frequency domain. The first type focuses on manipulating pixel intensity directly, which is applied in this project. Brightness contrast stretching is conducted using $s=T(r)$, where r is the grey level of the pixel (x, y) before image enhancement; s is the grey level of the pixel (x, y) after image enhancement. Figure 2.4 shows the brightness contrast stretching process, which receive an image as the input and generate an enhanced version of this image as the output using computational algorithm. The contrast enhancement is determined using the transformation of $s=T(r)$ to stretch the gray level of the object of interest. It creates better visibility of a particular range of gray level that corresponds to the object to be studied [50]. This stretch of gray level range is illustrated in Figure 2.5.

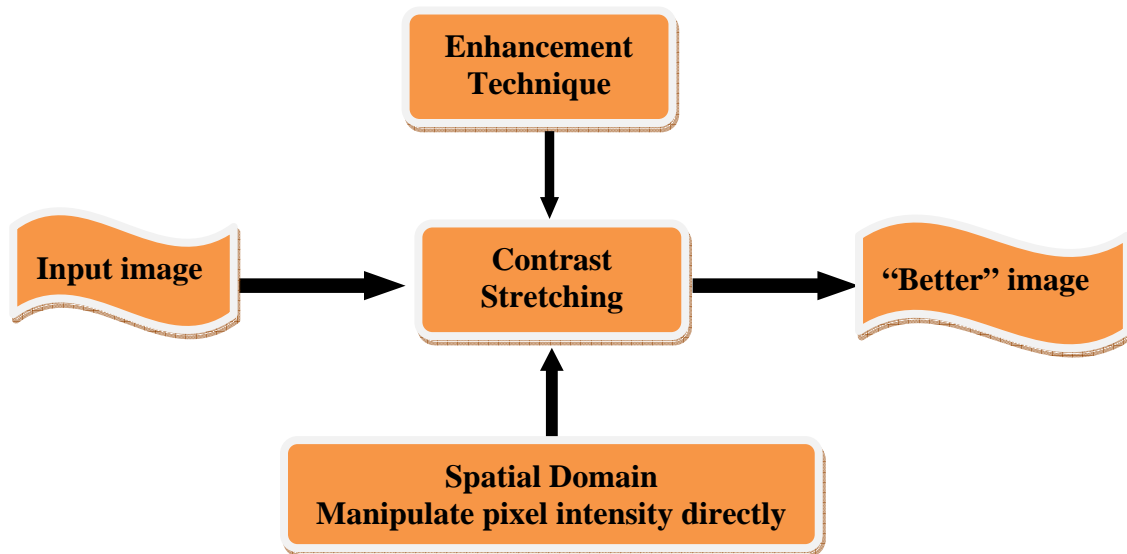


Figure 2.4 Image enhancement via contrast stretching

As can be seen in Figure 2.5, the shape of the transformation applied for contrast stretching is controlled by values of (r_1, s_1) and (r_2, s_2) . In practice, these values are usually

selected such that the interval $[s_1, s_2]$ covers the gray level range of the object of interest, and the interval $[r_1, r_2]$ provides the desired range of gray level for a better visibility of the object in the target image. Contrast enhancement is applied in this project and example results for the image enhancement are displayed as Figure 2.6. In the figure, (a) and (c) are abdominal regions. (b) and (d) are the enhanced pelvic bones. Visually, the pelvic bone regions in (b) and (d) appear much brighter than (a) and (c), which indicate the enhanced information of pelvic bone regions. At the same time, the soft tissues and other organs become darker. The contrast enhancement is performed here to stretch the gray level of the bones and allows them to be the main focus of the analysis.

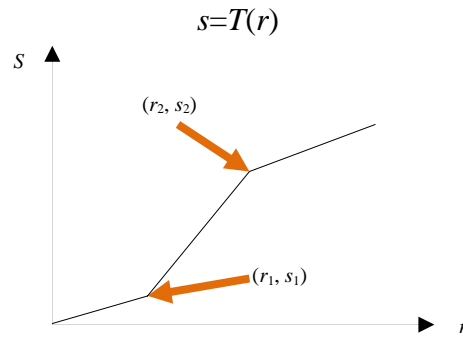
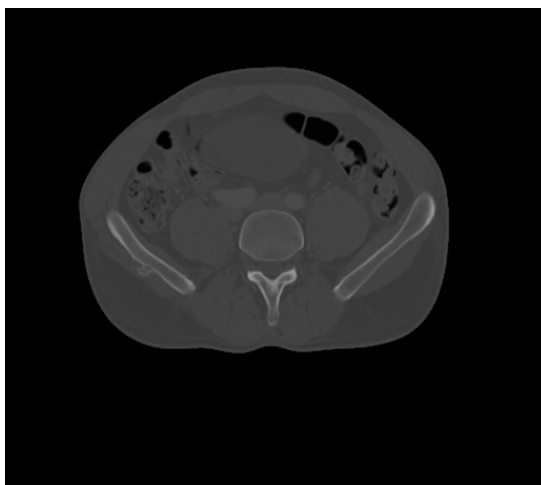
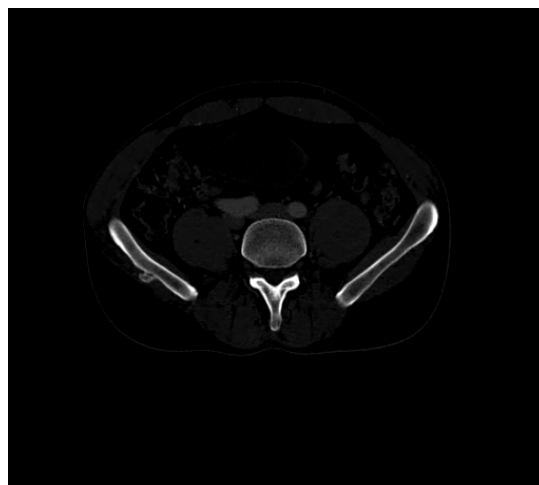


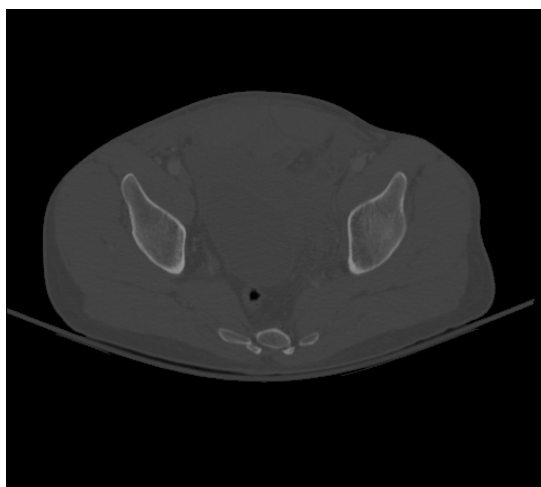
Figure 2.5 Contrast enhancement processing



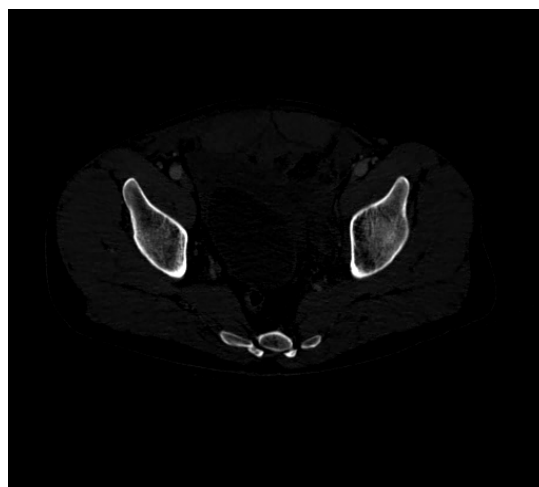
(a) Abdominal region example A.



(b) Enhanced pelvic bones example A.



(c) Abdominal Region example B.



(d) Enhanced pelvic bones example B.

Figure 2.6: Example results for the image enhancement.

2.4 *Edge Detection*

Edge detection is a fundamental tool in computer vision. In medical image processing, it is necessary to identify the boundary between the objects and separate the objects from each other. The edge of the image is the local area whose brightness changes significantly. The identification and extraction of the edge is very important for recognizing and understanding the entire image. Detected edges are normally the important features for image segmentation.

Edge detection techniques have been developed since 1959. Currently, there are many different edge detection approaches, such as Sobel edge detector, Canny edge detector and Laplace edge detector. The result of applying an edge detector to an image may lead to a set of connected curves that indicate the boundaries of objects. Apply the Laplacian edge detector often creates double borders; while other edge detectors, such as the Sobel edge detector, sometimes may not form a closed region. The Canny edge detector [51], uses a multi-stage algorithm to detect a wide range of edges in images.

In the proposed method, once the image enhancement is conducted, a series steps are taken for preliminary bone tissue segmentation, including Canny edge detection technique to detect the edges of bone tissue, morphological operations to remove spurious edges and sub-edges connection and removal. Figure 2.7 shows the schematic diagram for the entire edge detection process. The steps for edge detection are explained below.

- Step1: Canny detector is applied to obtain the preliminary edges.
- Step2: Morphological operations are performed to remove spurious edges and to make the bone edges continuous and smooth. Figure 2.8 shows an example of removing

spurs.

- **Step3:** The start and end pixels of each sub-edge are detected if there still remain a few disconnected edges. If there are less than 3 (where the number “3” was determined empirically) discontinuous pixels between the start and end pixels, a loop is formed to make them continuous. If the number of connected pixels of each sub-edge is less than three, it is considered isolated and those pixels are removed from the image.

In Figure 2.9, example results of edge detection are given. Figure 2.9 (a) and (c) show examples of the original pelvic CT image. Figure 2.9 (b) and (d) are examples of edge detected pelvic bone. More results are shown in Chapter 6. The obtained preliminary segmentation results are used for detecting the best matching template, which is described in following chapter.

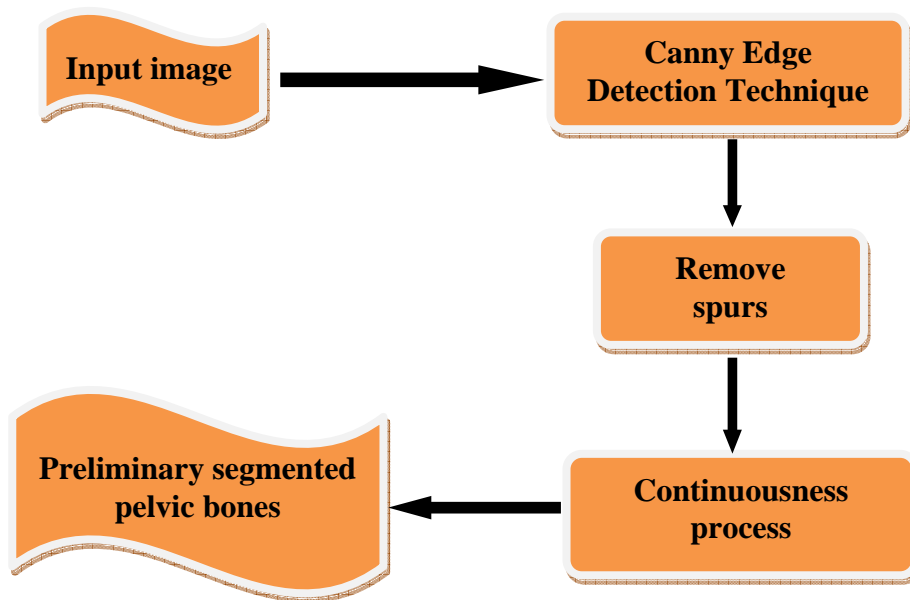


Figure 2.7 Schematic diagram of preliminary pelvic bone segmentation.

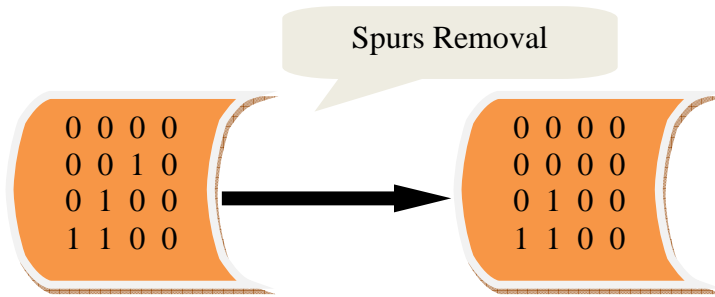
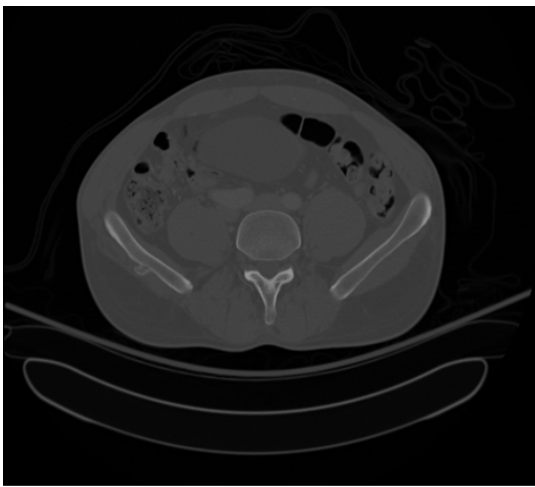
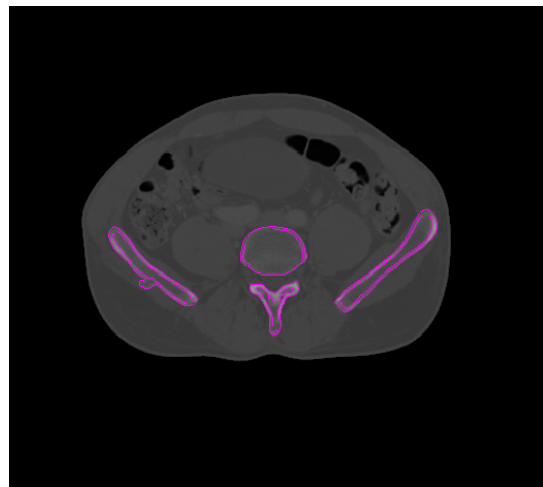


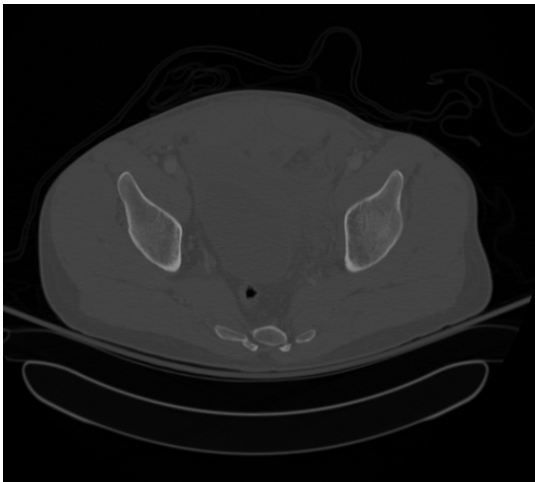
Figure 2.8: Spurs Removal Process.



(a) Original pelvic CT image example A.



(b) Edge detection of pelvic bone example A.



(c) Original pelvic CT image example B.



(d) Edge detection of pelvic bone example B.

Figure 2.9: Example results for the edge detection.

2.5 Summary

In this chapter, the methodologies for pre-processing and edge detection were introduced. The pre-processing steps eliminate the surrounding artifacts of the pelvic bone region and extract the bone. Image enhancement is carried out via the brightness contrast stretching process, which makes the pelvic bones distinguished and shows them in a highlighted way. Preliminary bone segmentation is then conducted utilizing the Canny edge detection technique. The results for each section were given.

CHAPTER 3 Methods for Shape Matching and Best Template Detection

3.1 Overview

In the project, the proposed bone segmentation algorithm is designed that conducts segmentation entirely automatically. This avoids human interference during the segmentation process, and therefore reduces some of the human-caused errors and inaccuracies during the diagnostic process. Also, automatic segmentation process can help the physicians reduce the decision-making time, which is highly important for traumatic pelvic injuries, especially in urgent cases such as the patient having severe hemorrhage. This chapter starts with describing the theoretical foundations of the Shape Matching algorithm, and then it follows by explaining the application of Shape Matching algorithm in the automatic bone segmentation process.

3.2 Shape Matching

In computer vision, shape matching is a fundamental step in many applications. A survey of shape matching methods can be found in [52, 53]. Shape matching approaches can be divided into two categories: (1) feature-based approaches which make use of spatial arrangements of extracted features such as edge information, and (2) brightness-based approaches which directly use pixel brightness information. The feature-based approaches focus on the boundaries of silhouette images that do not include the internal marking and holes, and are represented only by a single-closed curve. These methods, due to these restrictions, result in losing some important information. Related work, based on Fourier

descriptors, can be found in [54, 55]. Graph structure, as another example of this family, is utilized in feature based representation methods, as shown in [56, 57].

Huttenlocher et al. also developed methods based on Hausdorff distance [58]. Recently a wavelet based method has been developed to extract density from shape points, showing good results in [59]. The second category of methods, based on brightness and intensity information, uses classifiers to classify different shapes [60]. Cootes applies a statistical model to iteratively match points based on intensity value [62]. Other intensity based methods use classifiers to classify different shapes [63]. The method in [61] uses simple sampling of shape, utilizing shape context descriptor to represent shapes. This method is very effective and robust to deformation, outliers and noise. Moreover, it does not require strictly as curve or contour as an input, i.e. it does not assume that all segmented shapes form a single connected curve or contour, and is therefore adopted in this project.

A brief description of modified version of Shape Matching algorithm in [61] is given in this section. Two images are used for shape matching. The first image is the detected edge of each analyzed slice and the second image is one of 100 bone templates. The 100 anatomical bone templates for shape matching are created through manual selection of the bone regions from part of the male case of the Visible Human Project dataset [64]. These templates are from a male donor. In order to increase the segmentation accuracy, a female volunteer can be included in template matching process. This will ensure that the template matching process is more robust, and also the proper and correct bone templates will be matched to the input. In general, the bones of males are “larger and

more robust” than females, according to the Smithsonian National Museum of Natural History. Also, male bones tend to be thicker, especially at the places where muscles attach.

These templates are compared to similar images of patients in order to determine the best matched template. An overview of the algorithm is illustrated in Figure 3.1 and each step of the algorithm is further described below.

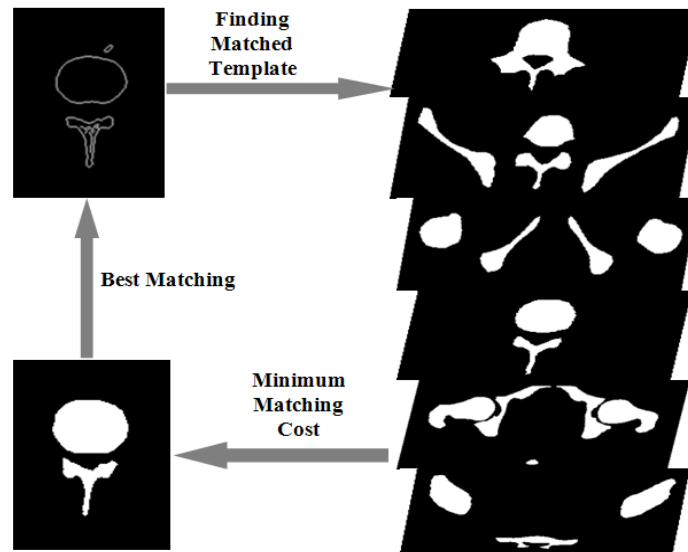


Figure 3.1: Shape matching process

- Step 1: A number of control points are selected automatically in each image to allow matching between the images. The matching between the objects in the template r and the preliminary segmented bone can be built based on these control points. First, n_1 control points on the edges of the objects in the segmented image and n_2 control points on the edges of the objects in the template image are sampled, because the edge points represent and describe the shape of object better than other points such as those inside the solid areas. The n_1 points on the segmented object and n_2 points on the template r object

represent a percentage of the total number of points around the edges of the objects in each image.

- Step 2: Once the controls points are selected for both the images, the shape context is determined for each point on the contour of the objects in the images. Shape context is a descriptor used for each selected point in the sampled shape as described in step 1. For each point p_i among the n_1 and n_2 control points on the shape of the corresponding objects in the segmented image and template r , the shape context of the point p_i is defined using a coarse histogram $h_i(k)$ of the relative coordinates of the remaining $n_1 - 1$ and $n_2 - 1$ points in the corresponding contours as defined in (3.1):

$$h_i(k) = \#A \{q \neq p_i \mid q - p_i \in \text{bin}(k)\} \quad (3.1)$$

where $\text{bin}(k)$ is a region encompassed by two rays and two radii, and for any set A, $\#A$ is the number of sample points in the set A. This histogram defines the shape context of the point p_i . The histogram bins are uniform in a log-polar space, making the descriptor more sensitive to the positions of nearby sample points. Figure 3.2 shows an example of the log-polar bins used to compute the shape context.

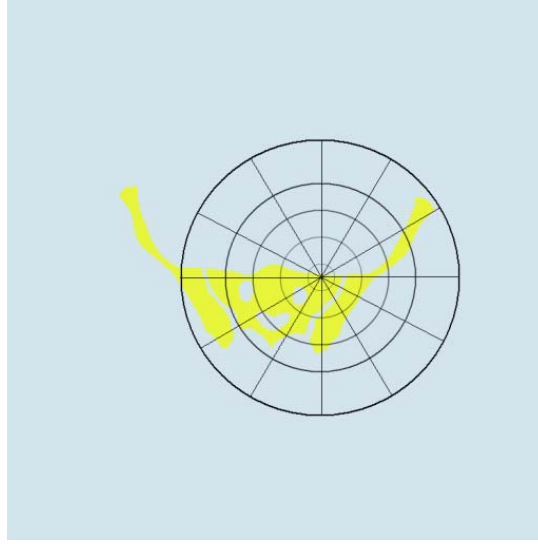


Figure 3.2: Diagram of the log-polar bins used to compute the shape context.

- Step 3: The matching cost for each individual point is determined. After computing all the shape context descriptors, consider a point p_i in the detected edge, and a point q_j in the template image, the cost of matching a point is as follows:

$$C(p_i, q_j) = \frac{1}{2} \sum_{k=1}^K \frac{[h_i(k) - h_j(k)]^2}{h_i(k) + h_j(k)} \quad (3.2)$$

where $h_i(k)$ and $h_j(k)$ are the K -bin normalized histograms at p_i and q_j , respectively. This function determines the matching between any pair of points on the contours of the two objects and allows quantitative assessment of the fitness of any pairing.

- Step 4: The matching cost between shapes in the segmented image and the template is determined. The overall cost of a match between the shape in the segmented image and the shape in the template image is the result of minimizing the sum of all individual point cost matches.

This process is repeated for all the 100 bone templates. After the best matched template is found, the corresponding training shape models of each best matched template can be directly applied to the preprocessed image for bone segmentation described in next Chapter.

3.3 *Summary*

The introduction of shape matching was given in the first part of this chapter. Next, the Shape Matching Algorithm applied in this work is described. This method is used to match the detected edge to every one of the available bone templates to find the best matched template. Sample results of shape matching were provided.

CHAPTER 4 Methods for Registered Active Shape Model

4.1 Overview

The last step of the segmentation method is explained in this Chapter. In this project, the Registered Active Shape Model (RASM) is proposed that can segment the pelvic bones from CT images automatically and accurately. Also, a novel initialization process is proposed for RASM using image registration and homogeneity features extracted from pelvic bone. This portion of the work was previously published in [77]. After pelvic bone structures are extracted from 2D CT images, 3D pelvic bone models are created based on continuous segmented bones in each slice. Two suitable evaluation measures to evaluate the final segmentation performance are defined as well. A cross-validation process is designed to validate reliable performance of the training models.

First, a review of Active Shape Model algorithm is presented, which is followed by a brief description of image registration techniques. The image registration method applied in this project is then presented in detail that includes the description of the homogeneity feature extraction algorithm. Later, the proposed RASM algorithm and the proposed automatic initialization approach for RASM are explained in detail. The proposed initialization process involves image registration and bone feature extraction as well as edge detection to sequentially and automatically place the training models of each individual object for the test images to extract the bone region from the background. Next, isosurface method is applied for 3D pelvic bone model creation based on 2D bone segmentation results. Mis-segmented Area and Mean Distance are separately defined to

evaluate the segmentation results. The cross-validation process for the training models is explained. Sample results for each step are given.

4.2 *Active Shape Model*

Active Shape Model [62] is a supervised learning technique that requires a set of labeled training images. The structure of interest in these images is represented by a series of landmarks manually placed along its boundaries. The statistical model of the desired structure is formed by extracting the shape and intensity information across the training set. This model is used to evaluate the possible deformation of each structure as the algorithm searches for the same structure in the test new images.

The first step in constructing the shape model is to determine a set of n landmarks, which describe the structure of interest in every training image. A given object can be represented as a $2n$ element vector x given by $x=[x_1, \dots, x_n, y_1, \dots, y_n]$, where (x_i, y_i) provides the coordinates of landmark x . ASM uses an iterative approach that sets the model parameters b to the mean shape of x , i.e. \bar{x} . Principle Component Analysis (PCA) is used to reduce the dimensionality of the dataset. x_i can be approximated by:

$$x_i \approx \bar{x} + Pb \quad (6.1)$$

where, P contains the eigenvectors of the PCA covariance matrix. Shape in this frame is defined by b ; x is aligned with a new set of image points Y (representing the shape in a new image). The image points are then projected into the model space so that the parameters in b can be updated to match them. The process is repeated until there is no significant change in b between iterations.

4.3 Image Registration

Image registration is the process of transforming different sets of data into the same coordinate system [70]. Data may be from different sensors, different times, or different viewpoints. Image registration is widely used in the fields of computer vision, medical imaging, pattern recognition, and remotely sensed data processing, and is a fundamental technique in comparing and integrating the data obtained from different measurements.

Due to the diversity of images to be registered and various types of image degradations, designing a general method for all registration tasks is very challenging. The method must take into account the assumed type of geometric deformation between the images, noise corruption, required registration accuracy and dependent data characteristic as well as other factors. However, most of the registration methods are composed of the following four steps.

- Feature detection. The main features such as edges, contours, corners, etc. are manually or automatically detected for further processing.
- Feature matching. In this step the correspondence between the features detected in input image and those detected in the reference image is established.
- Transform model estimation. The type of mapping functions as well as their parameters is estimated to align and map the input image with the reference image.
- Image resampling and transformation. The input image is transformed by mapping functions. Image values in the non-integer coordinated are computed by the appropriate interpolation technique.

Image registration is required in the proposed method in order to get robust training models from different patients with respect to their bone variations (translation, rotation, scaling, etc.). The image registration in this project consists of these steps: enhanced homogeneity feature extraction from each training image [8], correlation coefficient calculation for similarity measure, affine transformation, and Powell algorithm for optimization. Homogeneity, in this project is defined as a composition of two components: standard deviation and discontinuity of the intensities. Standard deviation describes the contrast within a local region in the image and discontinuity measures the abrupt changes of gray, which is obtained using edge detection.

Suppose s_{ij} is the intensity of a pixel P_{ij} at location (i, j) in an $M \times N$ image, and w_{ij} is a size $d \times d$ window centered at (i, j) .

The standard deviation of pixel P_{ij} is defined as:

$$s_{ij} = \sqrt{\frac{1}{d^2} \sum_{p=i-(d-1)/2}^{i+(d-1)/2} \sum_{q=j-(d-1)/2}^{j+(d-1)/2} (g_{pq} - \mu_{ij})^2} \quad (6.2)$$

where $0 \leq i, p \leq M-1, 0 \leq j, q \leq N-1$

$\mu_{i,j}$ is the mean of the gray levels within window w_{ij} , and is defined as :

$$\mu_{ij} = \frac{1}{d^2} \sum_{p=i-(d-1)/2}^{i+(d-1)/2} \sum_{q=j-(d-1)/2}^{j+(d-1)/2} g_{pq} \quad (6.3)$$

Discontinuity is calculated using Sobel edge detector and it use the magnitude of the gradient as the measure:

$$e_{i,j} = \sqrt{G_x^2 + G_y^2} \quad (6.4)$$

where G_x and G_y are the components of the gradient in x and y direction.

Then the two values are normalized and Homogeneity value is determined:

$$S_{ij} = \frac{s_{ij}}{s_{\max}}; s_{\max} = \max\{s_{ij}\} \quad (6.5)$$

$$E_{ij} = \frac{e_{ij}}{e_{\max}}; e_{\max} = \max\{e_{ij}\} \quad (6.6)$$

$$Homo(i, j) = 1 - E(i, j) \times S(i, j) \quad (6.7)$$

Since the bone tissues in pelvic CT images have higher intensity values, they appear brighter than other regions in the CT images. From the definition of Homogeneity value defined above, it can be seen that, the greater the intensity difference between a pixel and its neighbor pixels within the window of size $d \times d$, the smaller the value of Homogeneity. This allows the bone tissues to be effectively recognized and extracted for registration.

Figure 4.1 shows the flowchart of the entire proposed image registration algorithm. Figure 4.2 show the results obtained by Homogeneity extraction from the original images. The results show that the Homogeneity features of bone tissue are clearly detected and the bone shapes are precisely represented. Also, other objects like soft tissues are removed. In Figure 4.2, (a) and (e) are the original pelvic CT images, (b) and (f) are the images based on the Homogeneity feature extraction from (a) and (e), (c) and (g) are brightness enhanced images and brightness is adjusted shown in (d) and (h). The Homogeneity features are utilized for further image registration, which is described in next section.

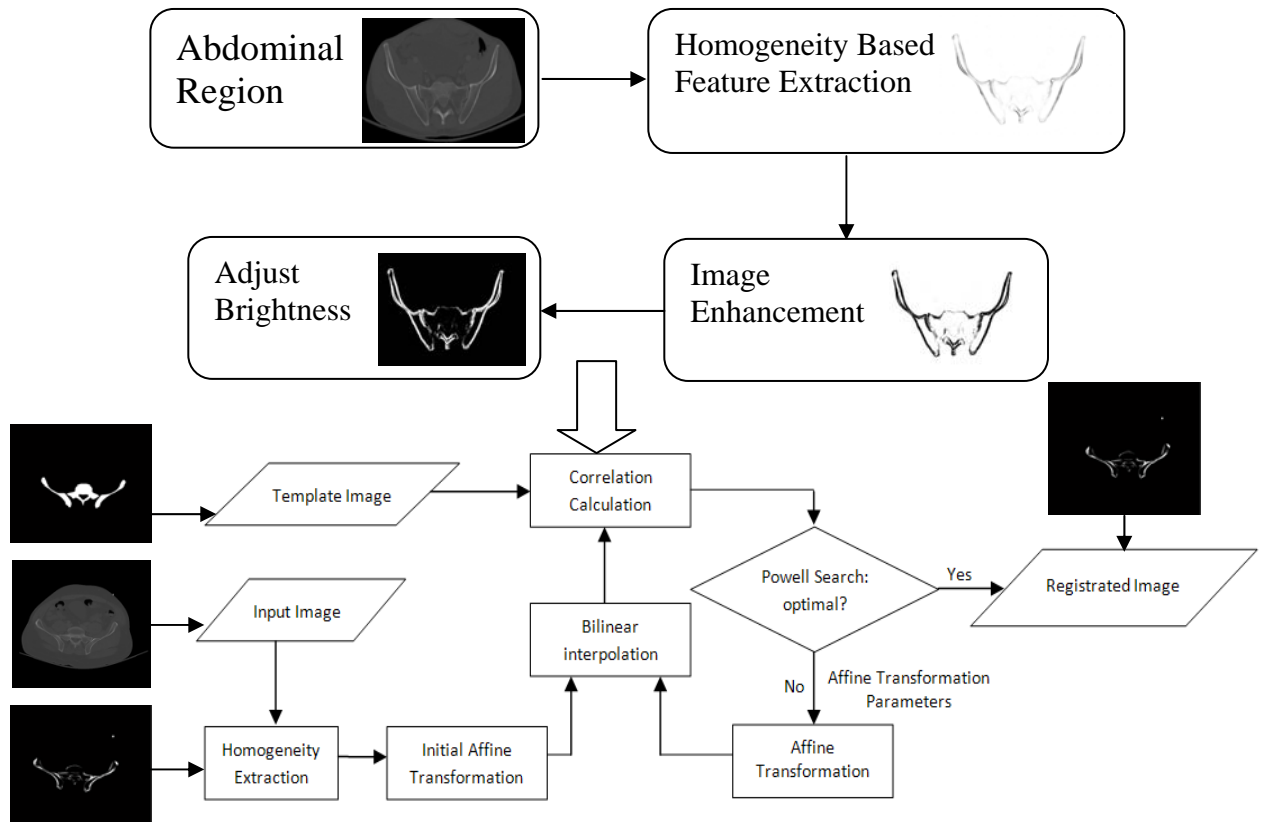


Figure 4.1: Image registration algorithm.

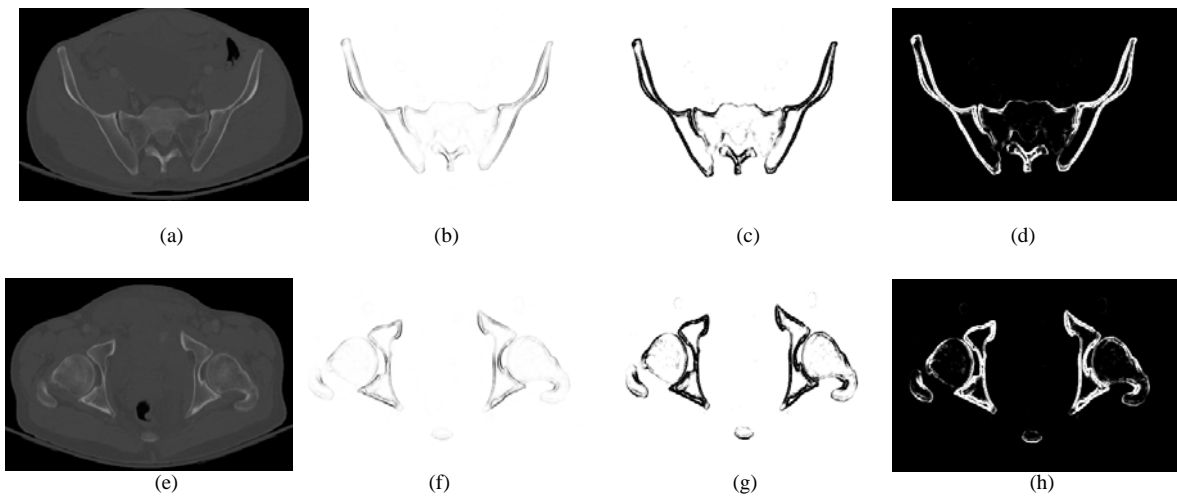


Figure 4.2: Example results for Homogeneity extraction

Figure 4.3 show the results of Homogeneity features based image registration. Visually, the size, location and rotation angle of the registered bone is more closely matched with the reference image rather than with the original input image (a). The maximum correlation value of 0.3947 is obtained through registration. Figure 4.3 (a) is the input image, (b) is reference image, (c) is the registered image. The affine parameters are: translation- 32, 5.25; rotation- 5; scaling- 1.028;

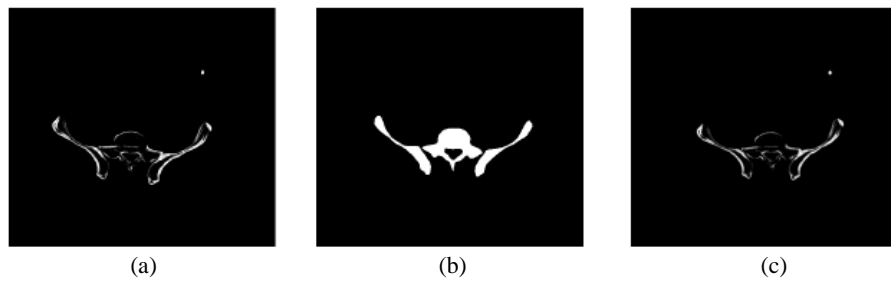


Figure 4.3: Example result of image registration.

4.4 Registered Active Shape Model

In general, the standard ASM uses training images labeled with landmark points to generate statistical shape and intensity-level models of a desired object. The shape model can be iteratively deformed to locate the object in a test image [62]. The landmarks are points selected by an expert for the bone region in each registered image during the training phase. Then, the algorithm attempts to fit the shape model to the object. However, the pelvic bones in each original training image have different sizes, rotation angles and locations that may lead to unstable and unreliable shape models for inaccurate bone segmentation.

In order to overcome this, in the proposed method, a new algorithm called Registered Active Shape Model (RASM) is formed using the image registration technique introduced in previous chapter combined with the Standard ASM. This algorithm, i.e. RASM, is developed to create a set of more robust training models which will result in better segmentation. For each level in pelvic CT scans, all the training images are registered to the template to create the registered shape models, the templates are the same as defined in Chapter 3. The entire RASM algorithm includes two stages: training stage in which registered training models are created, and the testing stage that includes automatic initialization. Figure 4.4 provides the flowchart for the RASM algorithm. After the creation of training models, segmentation is performed on the test images. Since manual initialization may fail to segment the targeted objects accurately, an automated hierarchical initialization algorithm is used in the study. The automatic initialization process is illustrated in next section.

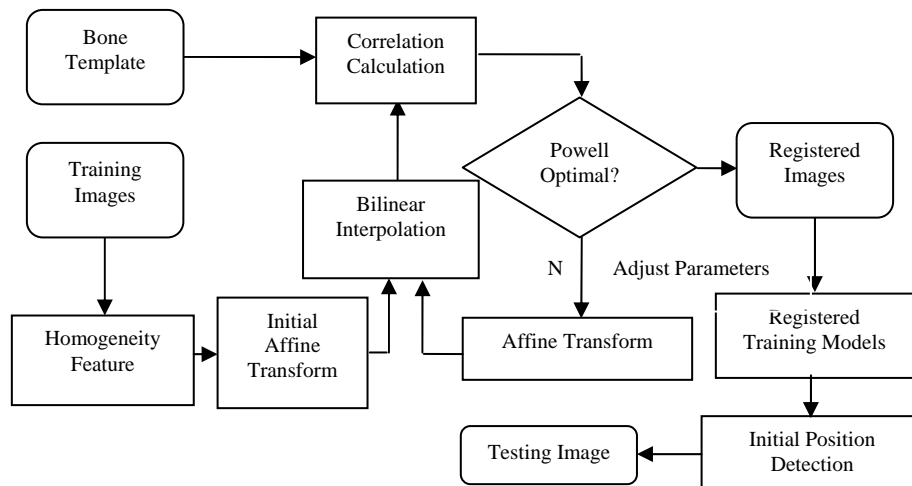


Figure 4.4: RASM Algorithm

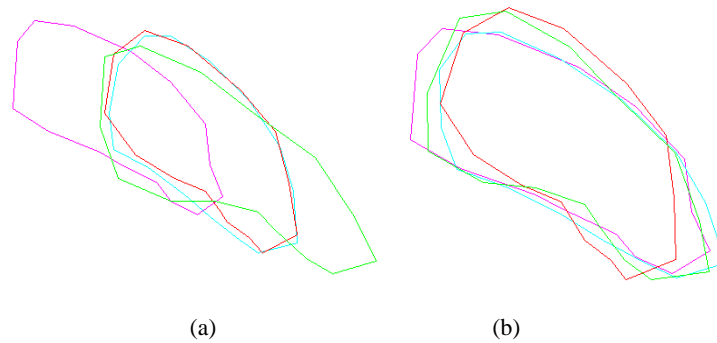


Figure 4.5: Comparison of results of standard shape model and registered shape model.

Figure 4.5 show the compared results of standard shape model and registered shape model. Figure 4.5 (a) is the shape model created from all training images without registration, (b) is the shape model created from all training images after registration. Visually, the bone regions in (a) are located in different initial positions while the bone regions in (b) are located closer to each other and within almost the same initial region. The size and rotation angles are also similar to each other, which allows the more robust shape model to be created.

4.5 Initialization for RASM

ASM takes a statistical approach that requires a set of labeled training images to determine variations of the desired shape in the testing new images. The standard ASM has been widely used in the recent years, but this method is highly sensitive to initialization. It requires that the initial position be correctly assigned to the training model in order to detect a target object in the image. Then the algorithm can attempt to fit the shape model to the object. If the shape model is not accurately placed, the Standard ASM method often fails to detect the target object.

This study addresses this shortcoming using a hierarchical initialization process that composes image registration, extracted bone features as well as prior edge detection results to sequentially place the training models for each individual object. This process avoids the need for manually indicating the initial positions. This will avoid human interference and reduce human-caused errors. The diagram of initialization process is illustrated in Figure 4.6. The diagram of segmentation using RASM and initialization process is shown in Figure 4.7. The algorithm is described as follows.

- Step01: Each training input image T_n is registered to corresponding anatomical template, where $n = 1, \dots, N$. N is the total number of training images.
- Step02: The coordinates for the landmarks in each bone structure are represented as $(x_{p,l}, y_{p,l})$, for $p = 1, 2, \dots, P$, $l = 1, 2, \dots, L$, where P is the number of bones, L is the number of landmarks for each bone. The mean shapes are obtained using RASM. The landmarks are the points selected by the expert to outline the boundary of bone region in each registered training image. During the training process for creating shape models, the uppermost position of each bone is taken as the starting landmark of the shape model.
- Step03: Centroid (C_p, D_p) is determined for all the mean shapes of the bones. All C_p values are sorted from the smallest to the largest.
- Step04: Test image E_m is registered to the corresponding template using homogeneity based image registration, where $m = 1, \dots, M$, and M is the number of test images.

- Step05: Pre-processing and Edge Detection methods are applied to the test image E_m to obtain the bone edges. The approximated contour of each piece of pelvic bone is detected.
- Step06: Centroid (C_p', D_p') is determined for all approximated contours of each piece of pelvic bone in test images. All C_p' values are sorted from the smallest to the largest.
- Step07: The corresponding relationship between these two groups of centroids (C_p, D_p) and (C_p', D_p') is achieved based on their sorted positions, through which the corresponding relationship between different training models and bones in test images is also achieved.
- Step08: The bounding box of each bone is determined for the test images.
- Step09: In the test images, within each box bounding, the corresponding training model is assigned the initial position with the uppermost position of the bone edge, then each shape model is correctly placed.

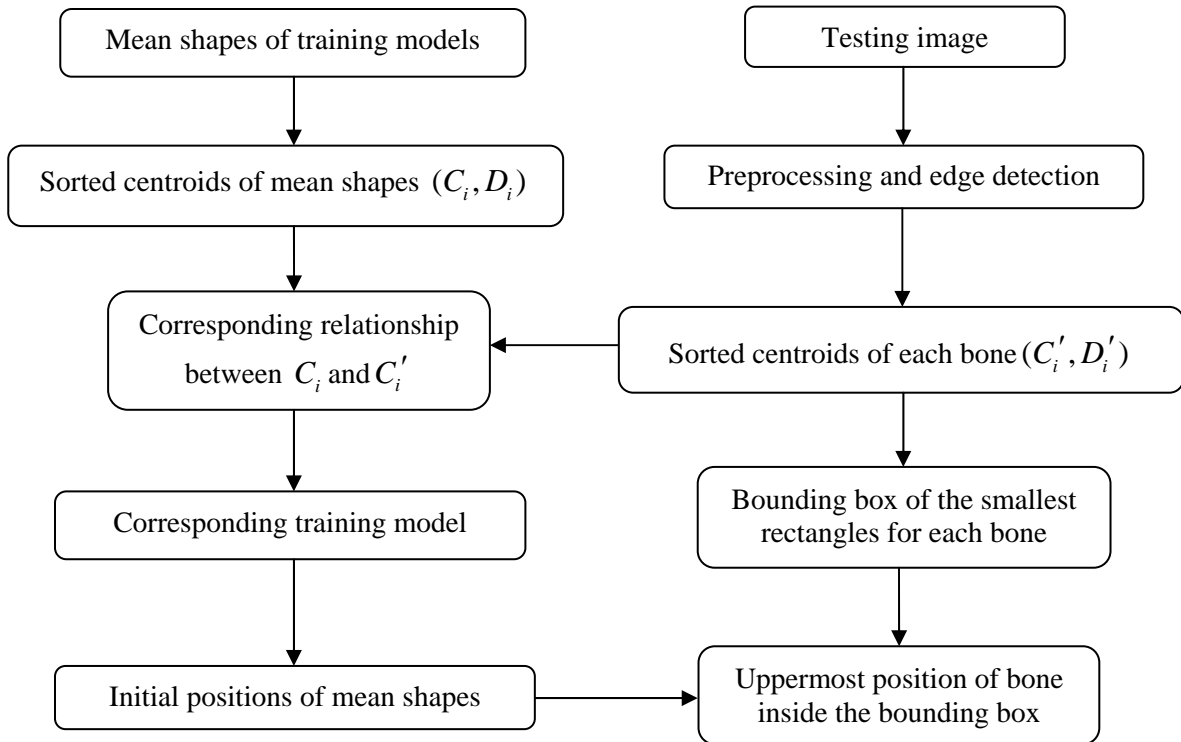


Figure 4.6: Proposed initialization process

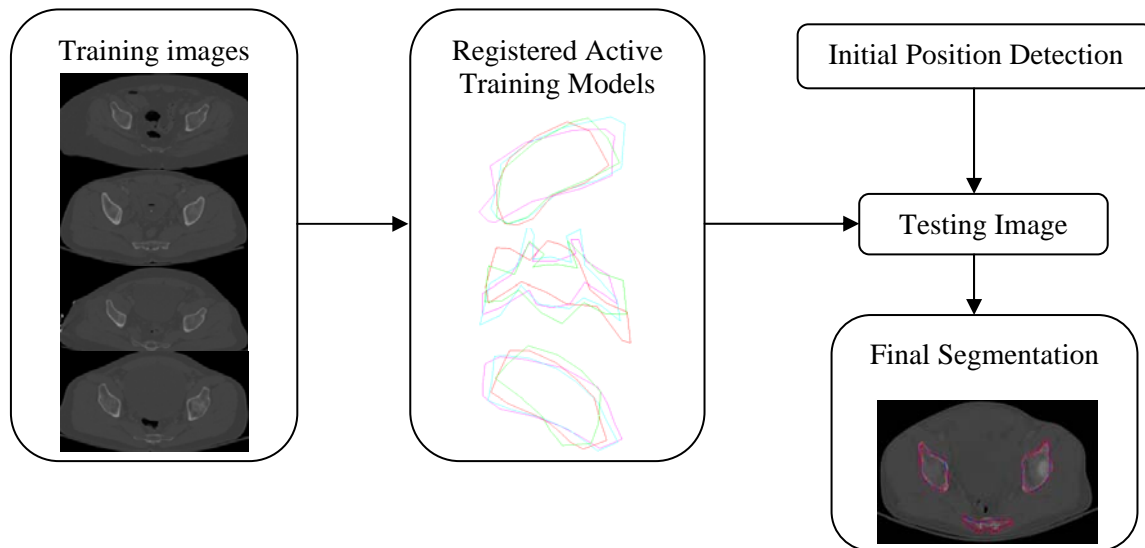


Figure 4.7: Diagram of segmentation using RASM and initialization process

4.6 3D pelvic bone visualization

The radiologists usually observe and analyze the patients' data with the combination of both 2D images and 3D models to make accurate diagnostic decisions in clinical diagnosis. In this dissertation, we apply the isosurface method to form the 3D pelvic bone models utilizing the segmented pelvic bones from 2D CT slices. In medical imaging area, isosurfaces may be used to demonstrate regions of a specific density in a three-dimensional CT scan. This method allows the visualization of organs, bones, or other structures. An isosurface is a 3D surface that represents points of an equal constant value within a volume of space-3D data distribution. Isosurface from the volume data is computed using the isosurface parameter specified. Isosurfaces are often used as data visualization methods, can be drawn on the screen very quickly.

After the 2D bone structures are extracted from continuous CT slices, we set a sphere in 3D domain as $\{x^2 + y^2 + z^2 = R^2\}$, a threshold as 0.5. The pixel value of all the non-bone regions including the background, soft-tissue and all other organs represented in CT images are set to 0, and the bone regions are set to 1. An isofurface is therefore formed based on the threshold value to separate the bone region in each layer from the background. The isosurface connects the points that have the equal pixel value and represent a 3D model of pelvic bone structure.

4.7 Summary

In this chapter, the final step of the proposed segmentation algorithm was stated, using Registered Active Shape Model (RASM) to automatically extract pelvic bone tissues from multi-level pelvic CT images. A novel hierarchical initialization process for RASM

was also introduced and demonstrated. Finally, the method for 3D pelvic bone model creation is explained.

CHAPTER 5 Fracture Detection and Displacement Measurement

5.1 Overview

This chapter presents the methodology for fracture detection. The entire hierarchical process consists of a series of steps, e.g. adaptive window creation, 2-D SWT application, masking, and boundary tracing is described. The sample results of fracture detection, including major fracture detection, minor fracture detection, and no fracture detection are described separately. Statistical measures, i.e. accuracy, sensitivity and specificity prove the superiority and effectiveness of the proposed methodology. The next section explains the approaches in detail. This portion of the work was previously published in [78, 79].

5.2 Methodology

Automated fracture detection is important for making fast and accurate decisions and treatment planning. In order to detect the pelvic bone fractures successfully, utilizing the bone information contained in pelvic CT images is very useful. After bone segmentation, a multi-stage process is used for fracture detection in the pelvic CT scans. Fracture detection of pelvic bones includes several steps. First, pelvic bone segmentation is conducted via the proposed RASM algorithm. The image is separated into two regions, along an approximated axis of symmetry. The information from these two regions is used to create two sets of multiple adaptive windows. Later, 2-D Stationary Wavelet Transform (SWT) is applied to each window to test the contour discontinuities in each window using

boundary tracing. If there is a contour discontinuity in a window, then it is considered as a potential bone fracture. Figure 5.1 presents an overview of the fracture detection process.

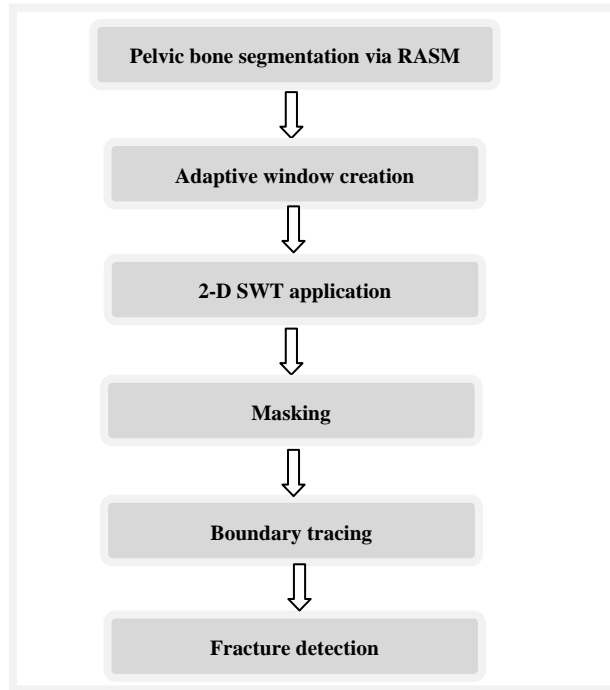


Figure 5.1: Schematic diagram of pelvic bone fracture detection

5.2.1 Adaptive Window Creation

Discontinuities around the bone boundary help identify the presence of fracture. Therefore, a detailed view of bone boundary is required. Creation of adaptive windows around the bone boundary will facilitate the process of identifying the discontinuities. Therefore, in this study, adaptive windows are created around the bone boundary to obtain a more detailed view of any discontinuities that may indicate fractures around the bone boundary. The appearance of bone fractures in a pelvic CT scan depends on the injury severity. Major fractures are usually visible while minor fractures may not severely distort the edge of the bone; instead they may appear as dual edges or a single sub-edge that is

slightly blurred compared to the neighboring edges. Therefore, it is important to refine the blurred boundary of each segmented bone in order to achieve accurate fracture detection. The refinement is done using a wavelet transform and edge detection which is later described in the following sections. However, due to local intensity variations, it may be difficult to achieve practical and desirable results by applying wavelet transform to the entire bone structure. Hence, the detected bone boundary is divided into a series of windows. The size and location of each window is determined by the area of the bone and boundary detected using the RASM. This is called adaptive windowing. The adaptive windowing algorithm is explained in detail as follows.

Based on the segmentation formed by the RASM algorithm, landmarks are placed on the boundary of each segmented bone. The algorithm starts from the first segmented pelvic bone region. The adaptive window is created based on each landmark placed on the segmented bone boundary. The size of each window is determined by the distance between each landmark and its previous landmark, as well as the distance between each landmark and its previous landmark. The location of each adaptive window is detected based on the landmarks around the entire bone boundary, i.e., adaptive windowing. The adaptive windows are created as follows.

The coordinates for the landmarks in each bone structure are represented as $(x_{p,l}, y_{p,l})$, for $p = 1, 2, \dots, N$, $l = 1, 2, \dots, M$, where, N is the number of bones, M is the number of landmarks for each bone.

The landmarks are located at the center position of each window. In order to ensure the size of the adaptive windows is suitable to cover the entire bone boundary, the length of the sides of the windows, $S_{p,l}$, is identified using (5.1), i.e.:

$$S_{p,l} = \frac{\sqrt{(x_{p,l-1} - x_{p,l})^2 + (y_{p,l-1} - y_{p,l})^2} + \sqrt{(x_{p,l+1} - x_{p,l})^2 + (y_{p,l+1} - y_{p,l})^2}}{2} \quad (5.1)$$

where $(x_{p,l-1}, y_{p,l-1})$ is the previous landmark of each landmark $(x_{p,l}, y_{p,l})$ and $(x_{p,l+1}, y_{p,l+1})$ is the next landmark of each landmark $(x_{p,l}, y_{p,l})$.

Since the area of each adaptive window is small, in order to obtain more suitable virtualization effects, each window is scaled to the size of 256×256 by applying a bilinear interpolation technique [67]. After adaptive windowing, 2-D Stationary Wavelet Transform (SWT), non-bone region masking and boundary tracing, as described later, are performed on each window. As shown in Figure 5.2, each landmark is located at the center of each window.

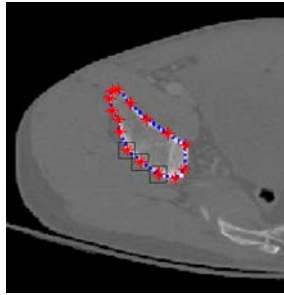


Figure 5.2: Example windows around the boundary of pelvic bone, positioned according to landmarks

5.2.2 The 2-D Stationary Wavelet Transform

After adaptive windowing, 2-D Stationary Wavelet Transform (SWT) is applied on each window in order to refine the blurred boundary of segmented pelvic bone. SWT is

applied in our work as it is designed to overcome any shift variation [13], the algorithm is explained as follows.

The wavelet transform decomposes an input signal into different frequency components using a series of filtering operations. A wavelet is a function $\overline{\varphi}_a(t)$ with a zero average.

$$\int \psi(t) dt = 0 \quad (5.2)$$

The wavelet generates a family of wavelets by scaling $\psi(t)$ by a and translating it by θ :

$$\varphi_{\theta,a}(t) = \frac{1}{\sqrt{a}} \varphi\left(\frac{t-\theta}{a}\right) \quad (5.3)$$

The wavelet transform of a signal $s(t)$ at time θ and scale a can be represented as:

$$W_s(\theta, a) = \left\langle s(t), \varphi_{\theta,a}(t) \right\rangle \quad (5.4)$$

$$W_s(\theta, a) = \int_{-\infty}^{+\infty} s(t) \frac{1}{\sqrt{a}} \varphi^*\left(\frac{t-\theta}{a}\right) dt \quad (5.5)$$

$$= x * \overline{\varphi}_a(\theta) \quad (5.6)$$

where $(*)$ represents the convolution and $\overline{\varphi}_a(t)$ is

$$\overline{\varphi}_a(t) = \frac{1}{\sqrt{a}} \varphi^*\left(\frac{-t}{a}\right) \quad (5.7)$$

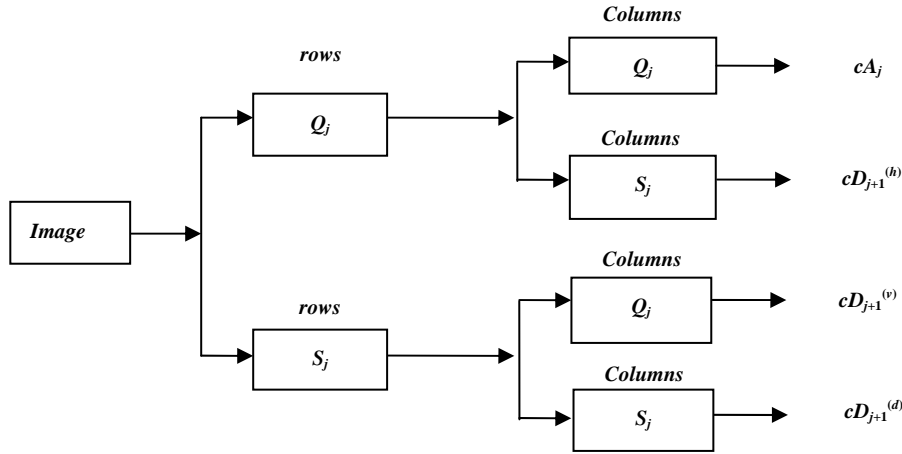
The convolution computes the wavelet transform of the input signal with dilated band-pass filters. Two sets of coefficients are obtained through wavelet transform, one is approximation coefficients, cA_j , and the other is detail coefficients, cD_j , where j is the level of decomposition, including horizontal, vertical and diagonal coefficients. Decimation

makes wavelet transform a shift-variant process, which means that classic wavelet transform of a translated version of a signal is not the same as the wavelet of the original. To overcome this shortcoming, stationary discrete wavelet transform is used in our study.

The scaled window W is first decomposed via the 2-D Stationary Discrete Wavelet Transform. The classical Discrete Wavelet Transform (DWT) is not a space-invariant transform. The SWT is an algorithm which does not decimate the coefficients at every level of decomposition [68]. The filters at level i are up-sampled versions of those at level $(i-1)$. As with the 2-D DWT, decomposition outputs approximation, horizontal, vertical and diagonal coefficients. In this application, three levels of decomposition are applied to window W using the Haar wavelet. The level 3 detail coefficients, $cD_{j+1}(h)$, $cD_{j+1}(v)$, $cD_{j+1}(d)$, are then extracted and used to reconstruct detail arrays D_h , D_v and D_d of horizontal, vertical, and diagonal coefficients. Figure 5.3 represents decomposition of 2-D SWT.

The accuracy and running speed are compared when extracting the up-sampled coefficients separately at 1st, 2nd, and 3rd level. The algorithm runs on the computer with 2.80GHz Intel(R) Core(TM) i7 processor, 64-bit Operating System, 6.0 GB memory. For each CT slice, it takes approximately 0.5 seconds more for the 2nd level of stationary wavelet decomposition than the first level decomposition. While, the 3rd level of decomposition is only 1 second slower than the 1st level of decomposition, in terms of running speed. More noise is filtered out and edges are clearer in the 3rd level of decomposition compared to other two levels; this improves the accuracy of our fracture detection algorithm. Going to the 4th level adds another 1.5 second of additional delay

while not adding much to filtering performance. Hence, in order to achieve the balance between the running speed and accuracy, the 3rd level of SWT is applied in our work.



where,

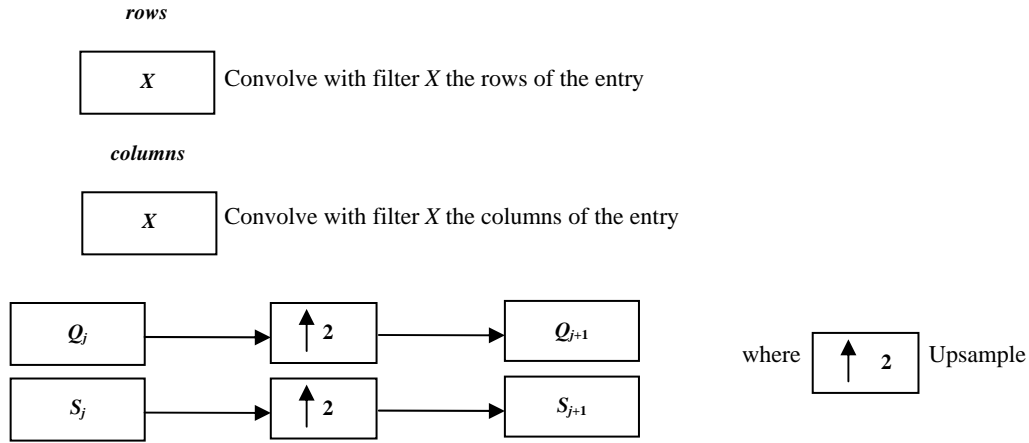


Figure 5.3: Decomposition steps of 2-D SWT.

5.2.3 Masking

The next step in the fracture detection is to create a binary version of the chosen detail coefficients from the wavelet transform W_b . This binary version not only contains the pelvic bone contour, but also includes other extra and unnecessary edges. A mask is formed to filter these redundant edges out. The mask W_m is formed by converting the

smoothed window to a binary image using Otsu's threshold [69]. The threshold is computed to minimize the intra-class variance, defined as a weighted sum of variances of two classes, black and white pixels.

$$\sigma_w^2(t) = w_1(t)\sigma_1^2(t) + w_2(t)\sigma_2^2(t) \quad (5.8)$$

Weight w_i is probability of each class separated by a threshold t and σ_i^2 is variance of each class. Minimizing the intra-class variance is the same as maximizing inter-class variance:

$$\sigma_b^2(t) = \sigma^2 - \sigma_w^2(t) = w_1(t)w_2(t)[\mu_1(t) - \mu_2(t)]^2 \quad (5.9)$$

where w_i is probability of each class and μ_i is the class mean.

The contour is then extracted from the binary image. The unwanted edges are removed from the binary image to create an edge window. Later, a precise edge window W_e is obtained by removing the extra edges in the image using the pelvic bone contour and the mask. The process is defined as a combination of W_b and W_m .

$$W_e = W_b \times W_m \quad (5.10)$$

5.2.4 Boundary Tracing

After masking, the last and final step in fracture detection is discontinuities detection. This is achieved by tracing the extracted bone edges. Sometimes, small artifacts surrounding the extracted bone edges may interfere with the boundary tracing. Therefore, these artifacts must be removed. These are removed by applying morphologic opening to all the objects in the image with area below a specific threshold. The remaining edges are then traced using the 8-neighborhood of each pixel and are returned as a matrix of pixel positions. The traced edges represent the pelvic bone contours. Depending on different

types of fracture and severity of fracture, if a fracture is present, then multiple boundaries can be identified in the selected window, then it is considered as a potential bone fracture. If the window has a single continuous boundary, then it is considered as no presence of fracture. Sample results of fracture detection are shown in Figure 5.4; more results detected from multi-slices of pelvic structure are shown in Chapter 6.

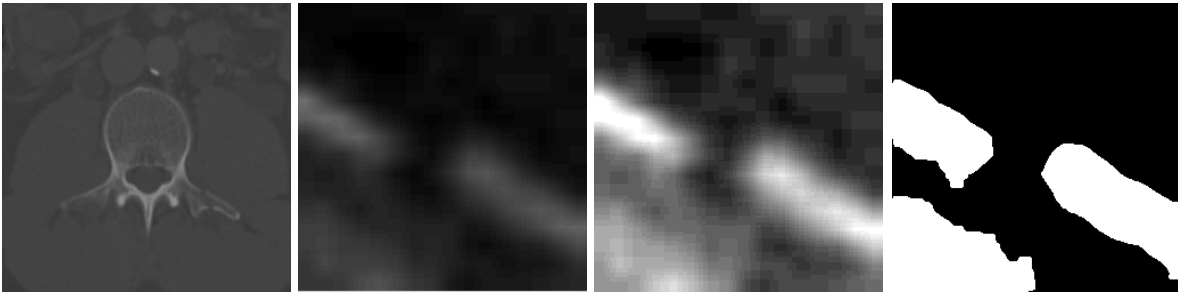


Figure 5.4: Sample results of fracture detection.

5.3 Quantitative displacement measure

The quantitative displacement measurement is important to determine the pelvic injury severity. For the above detected fracture, the displacement is determined by measuring the distance between the tips of the fractures bone. If (x_o, y_o) is the coordinate of a tip of one piece of the fractured bone and (x_s, y_s) is the coordinate of a tip of the other piece of the same fractured bone, the gap d is calculated as follows.

$$d = \sqrt{(x_o - x_s)^2 + (y_o - y_s)^2} \quad (5.11)$$

Due to the window scaling effect of the previous step, the gap d_a is calculated using 5.

$$d_a = \sqrt{(x_o - x_s)^2 + (y_o - y_s)^2} \times \frac{S_{p,l}}{256} \quad (5.12)$$

Figure 5.5 below shows the displacement measurement in the fractured bone.

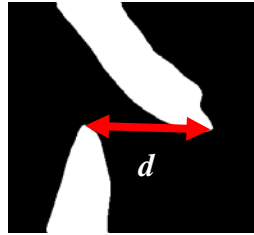


Figure 5.5 Displacement calculation

5.4 Summary

This chapter presented a hierarchical method for detecting fractures in pelvic bones using adaptive windowing, boundary tracing, 2-D Stationary Wavelet Transform and while including anatomical information. Also, the quantitative measure of fracture severity in pelvic CT scans was defined. The results show that the proposed method is capable of detecting fractures in pelvic bones. Automated fracture detection, once verified with more data, will be an invaluable component of a larger modular system to extract features from CT images for a computer-assisted decision-making system.

CHAPTER 6 Results of Image Processing

6.1 Overview

This chapter provides the results of the proposed segmentation and fracture detection methodologies. The results of these steps include eliminating surrounding artifacts and extracting the pelvic region, image enhancement, edge detection, matching to a template, homogeneity extraction, image registration, segmentation using RASM, 3D pelvic model creation, and segmentation of key structures using different training models. Results using Snake method and results using RASM are compared and shown separately. In each step, the results obtained based on multiple samples are presented. These samples represent different slices of the CT scans taken from different patients. The variations among these samples allow better assessment and evaluation of the system performance when dealing with different shapes of bone of different patients. The dataset is explained in next section.

6.2 Dataset

The dataset has been obtained from the Virginia Commonwealth University Medical Center. Data have been collected from twenty patients with traumatic pelvic injuries. Forty-five to one hundred-twenty nine images are collected for each patient, which represent a variety of anatomical structures within a pelvic CT scan and display similar structures within the group of patients. Axial CT images with one to five millimeter slice thickness are used for the study. Images collected from five patients are used for training and the other fifteen patients' images are used for testing. For fracture detection, a

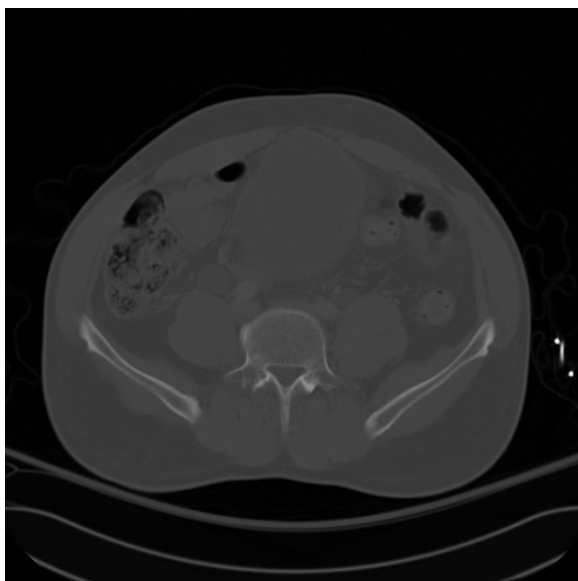
total of twenty patients are used, out of which fifteen patients exhibit small to very severe bone fractures. The total number of images used from these twenty patients is 1346.

6.3 Segmentation Results

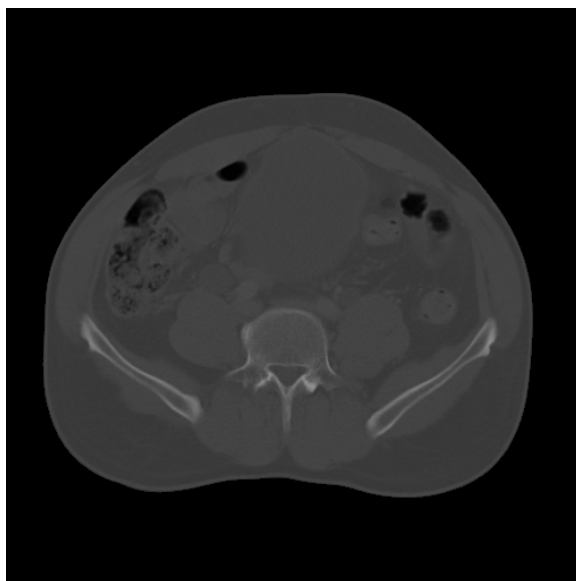
Results corresponding to different stages of the proposed methodology are presented in the following sections.

6.3.1 Results for eliminating surrounding artifacts and extracting the pelvic region

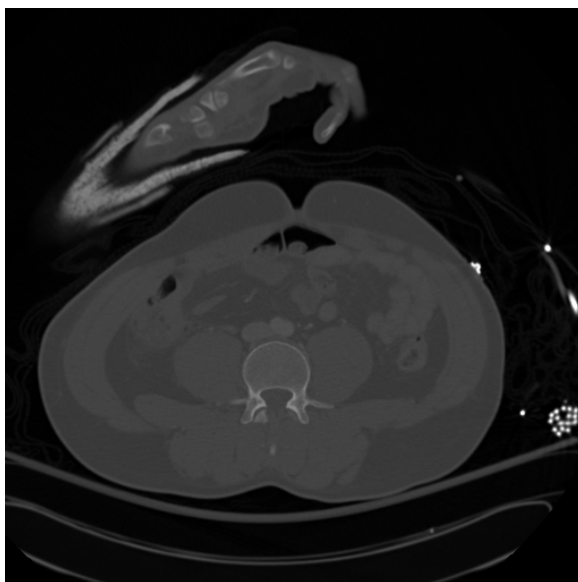
Figure 6.1 demonstrate the results of using the proposed pre-processing method to eliminate the surrounding artifacts such as the CT table and cabling. The inclusion of artifacts can influence the gray level statistics and make the segmentation process to be complicated. The results of removing the surrounding artifacts and extracting the pelvic region are evaluated visually and also by calculating the percentage of the removed area in total area of the objects in the original image. The mean area removed from each image in the testing dataset is approximately 6%. In Figure 6.1, the images in left column are the original images, it can be noticed that the cabling and other background objects exist in Figure 6.1 (a) and Figure 6.1(c). The images in right column show the results of eliminating cabling and other background objects which exist in (a) and (c), respectively. For all the test images, the method successfully eliminates the surrounding artifacts of abdominal regions.



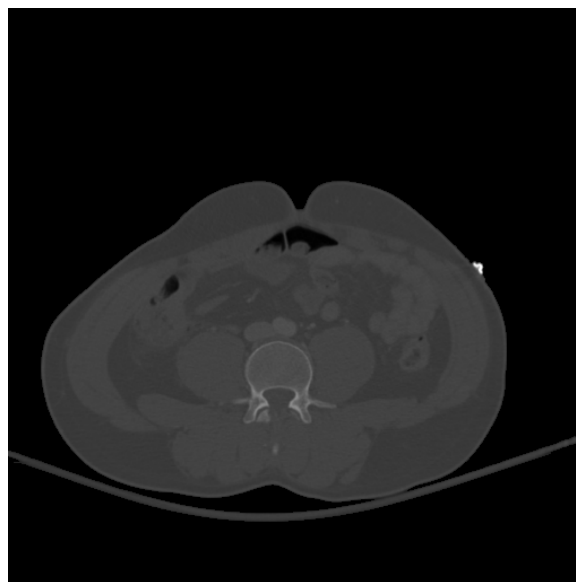
(a) Raw CT slice example A.



(b) Abdominal region after artifact removal example A.



(c) Raw CT slice example B.

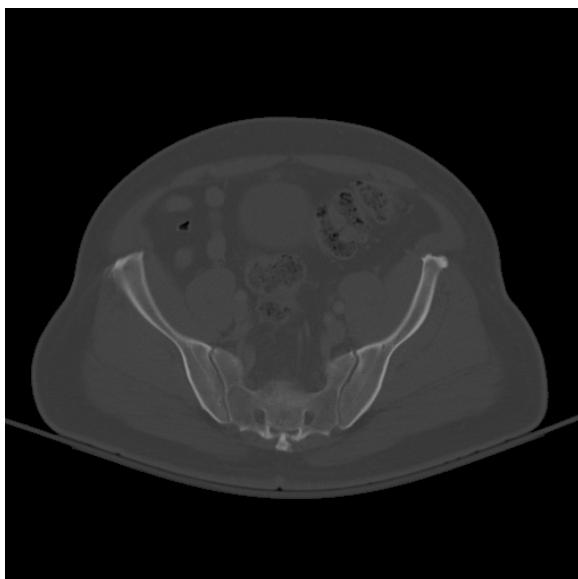


(d) Abdominal region after artifact removal example B.

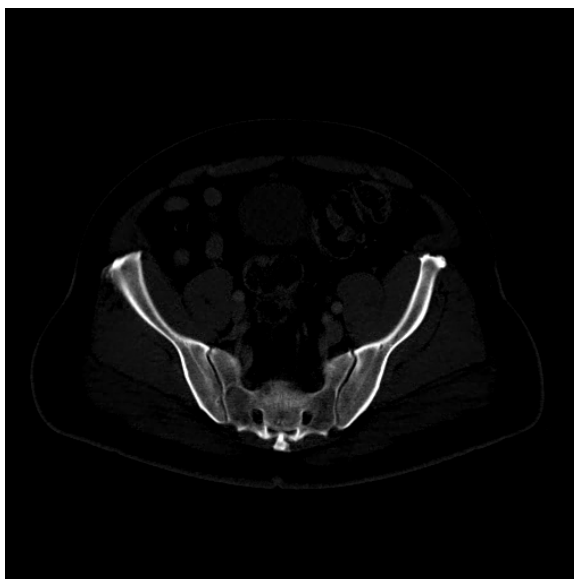
Figure 6.1: Sample results for extracting the pelvic region from the raw CT Image.

6.3.2 Results for image enhancement

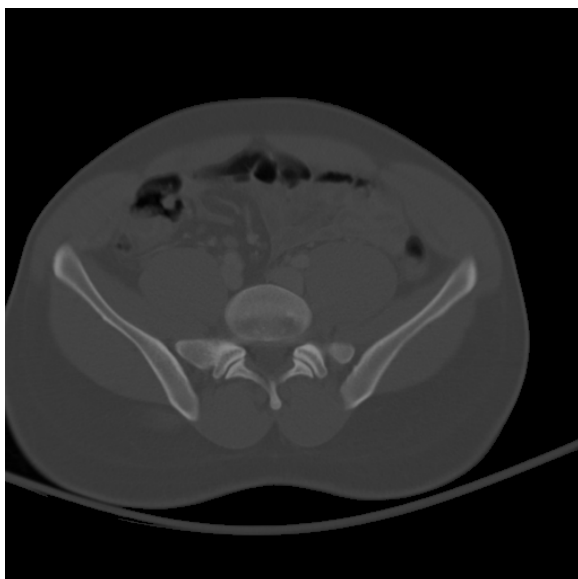
Examples of results produced by the method described in Section 2.3 are shown Figure 6.2. It can be seen in Figure 6.2 that the features of interest – the pelvic regions are emphasized in (b) and (d). These features appear much brighter for the image reviewers while simultaneously the non-interested features – soft tissues and other organs appear much darker compared with the bone regions. The results of image enhancement are evaluated visually. For the entire test dataset, the brightness of bone regions in all the test images is successfully adjusted and made brighter. The results will be used for better edge detection performance, which will be described in the next section.



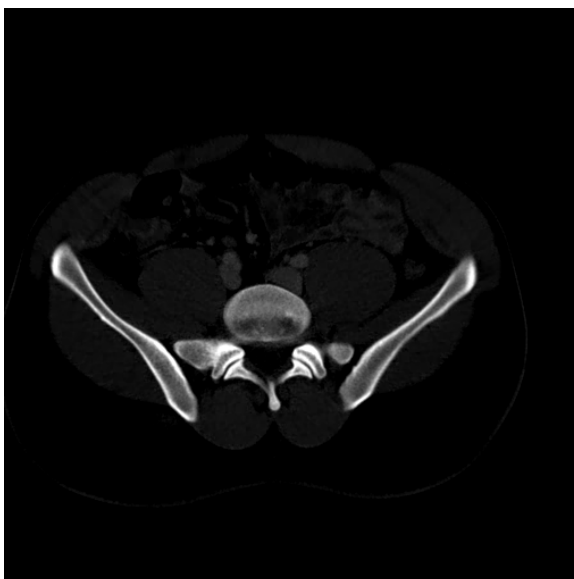
(a) Abdominal region after artifact removal example A.



(b) Enhanced image example A.



(c) Abdominal region after artifact removal example B.



(d) Enhanced image example B.

Figure 6.2: Example results for image enhancement.

6.3.3 Results for edge detection

Detected edges are normally the important features for image segmentation. This section shows the results of edge detection using the methodology described in Section 2.4. As shown in Figure 6.3, the images (a) and (c) in the left column are the enhanced images, the images (b) and (d) in the right column are the results of edge detection. The edges of pelvic bone regions are clearly defined. The results of edge detection are evaluated visually to see if the boundaries of pelvic bone regions are extracted completely. The validation process also tests if other non-bone regions are included during edge detection. For the entire test dataset, the edges in almost all of the test images are successfully extracted. However, by examining the results it can be observed that the connectivity of the bone tissues needs to be improved, as it can be seen in Figure 6.3(b). The next steps of the algorithm attempt to address these issues. The results will be used for matching a shape template in the next section.



Figure 6.3: Example results for preprocessing and edge detection

6.3.4 Results for matching a template to the analyzed slice

In this section, results produced by the shape matching algorithm are presented. Shape matching is used to associate a template with each slice. The association is made by selecting the template with minimal matching cost to the detected edge obtained from last section, which can make the entire segmentation process automated. Choosing the template with minimum matching cost proves to be a simple and efficient technique for creating an accurate association. Sample results for template matching using the shape matching method, presented in Chapter 3, can be seen in Figure 6.3. The shape matching method proved to be robust in choosing suitable templates. In Figure 6.3, the input image - detected bone edge (the upper left image) is compared with all 100 bone templates (template examples on the right side), and the template with minimum matching cost 26.6695 is achieved as the best matching template for the input image.

Evaluation of the matching results of all test images are compared with 2-D

TABLE 6.1
EVALUATION OF THE MATCHING RESULTS USING SHAPE MATCHING AND
CORRELATION COEFFICIENTS

Similarity Criterion	TOTAL NO. OF IMAGES	Total No. of accurately matched images	Accuracy
Shape Matching	675	598	0.859
2-D Correlation Coefficients	675	440	0.652

correlation method and shown in Table 1. The results show that shape matching method proved to get higher matching accuracy than 2-D correlation coefficients method. Evaluation of the results of shape matching suggests that the accuracy of the tested

templates were matched with a suitable template is 85.9%. Figure 6.4 shows the entire process of shape matching. Figure 6.5 show two more sample examples of best matched template for the analyzed slice.

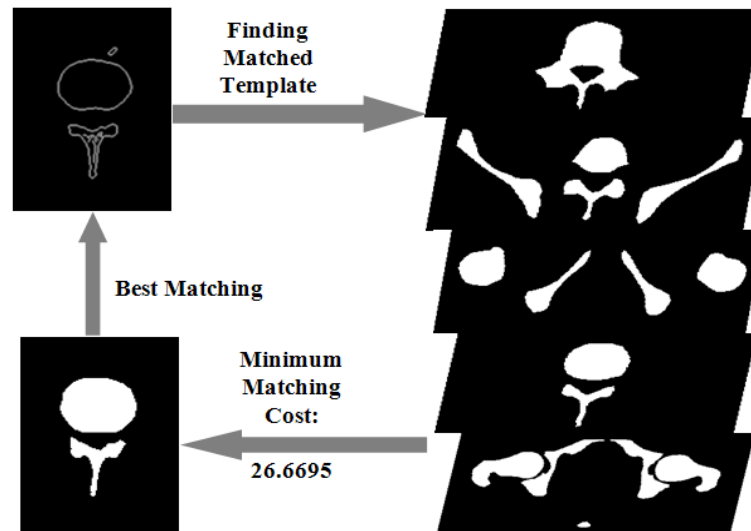


Figure 6.4: Example result of shape matching process

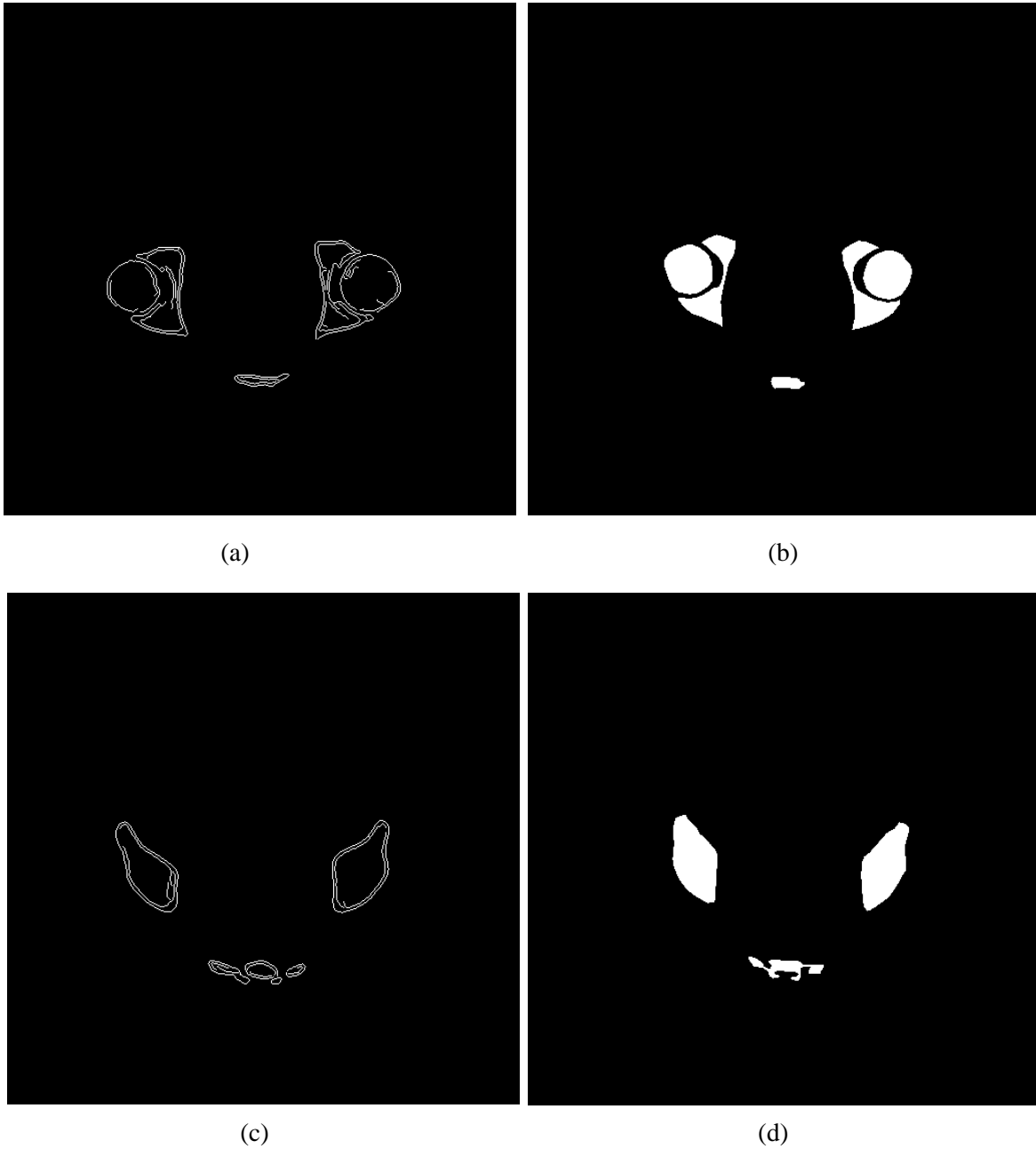


Figure 6.5: Example result of finding best matching Template

6.3.5 Results for Homogeneity Feature Extraction

Figure 6.6 shows the results obtained by homogeneity extraction from original images. The results show that the homogeneity features of bone tissue are clearly detected

and the actual contours of the bones are precisely represented. Also, other objects such as soft tissues are removed. In Figure 6.6, (a) and (e) are original pelvic images, (b) and (f) are the images based on homogeneity feature extraction, (c) and (g) are brightness enhanced images and brightness is adjusted shown in (d) and (h). The homogeneity features are utilized for image registration, as described in the following section.

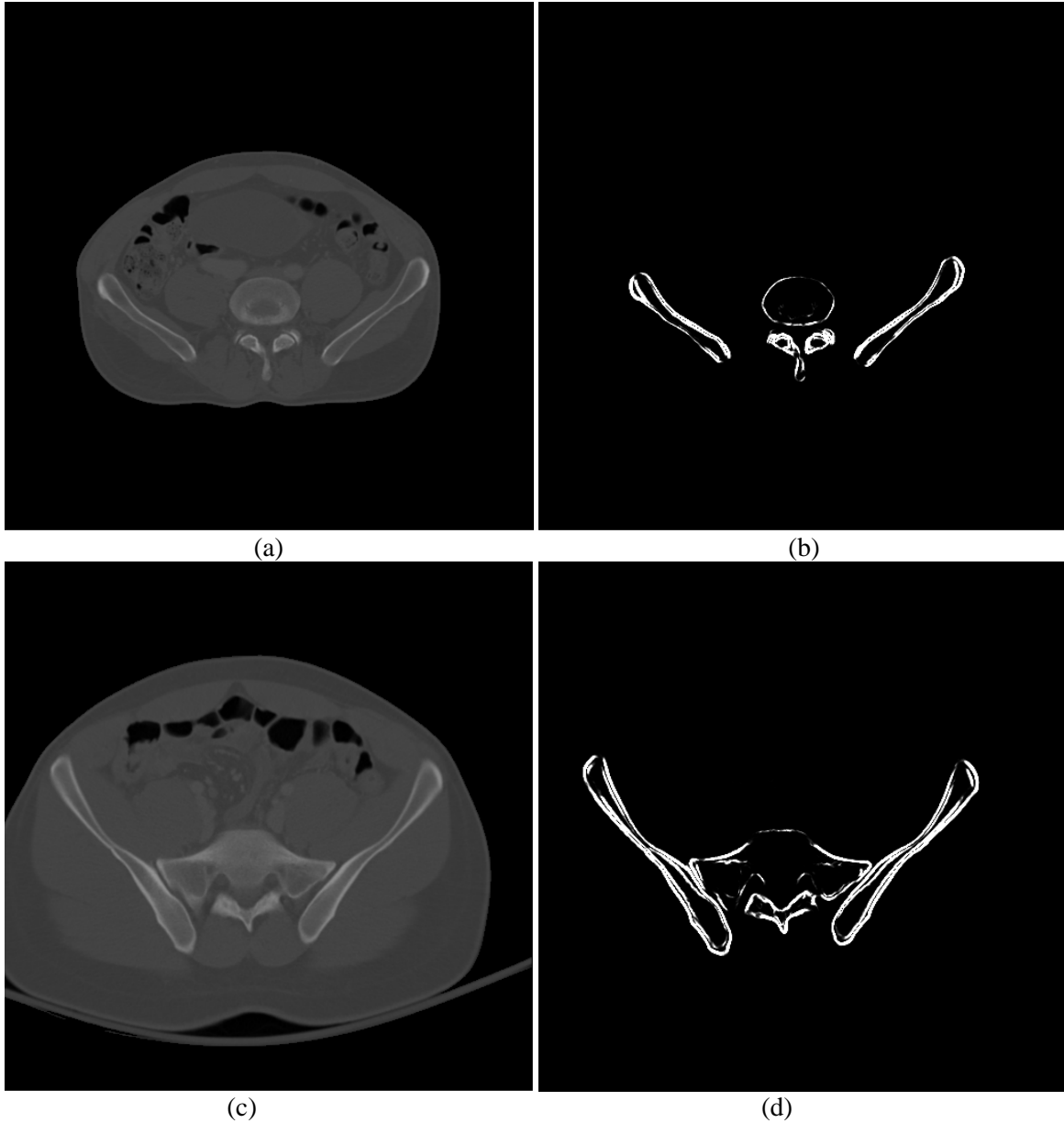


Figure 6.6: Example results for homogeneity extraction.

6.3.6 Results for image segmentation

Figure 6.7 shows the segmentation results based on RASM with the proposed initialization processing. The results show that the proposed method accurately segments the pelvic bones (lumbar, ilium, sacrum, femur, pubis, ischium). The initial positions of

training models are also detected accurately. Results of the Standard ASM for segmenting pelvic bone are shown in Figure 6.8. The initial positions of training models are not correctly assigned in test images, which may be the main reason of inaccurate bone segmentation. Figure 6.9 represent the example results of pelvic bone segmentation via Standard ASM with manual initialization, the method fails to detect the target bones. This is because the training models are created without registration that they are not robust enough to capture the variability of the bone structures in testing images.

The algorithm runs on MATLAB using a computer with a 2.80GHz Intel(R) Core(TM) i7 processor, 64-bit Operating System, and 6.0 GB memory. For each CT slice, it takes approximately six seconds to conduct automatic bone segmentation. For each CT scan, the average time efficiency for segmentation is eight minutes. The algorithm running in C++ runs much faster, and the total segmentation time for each CT scan is one minute.

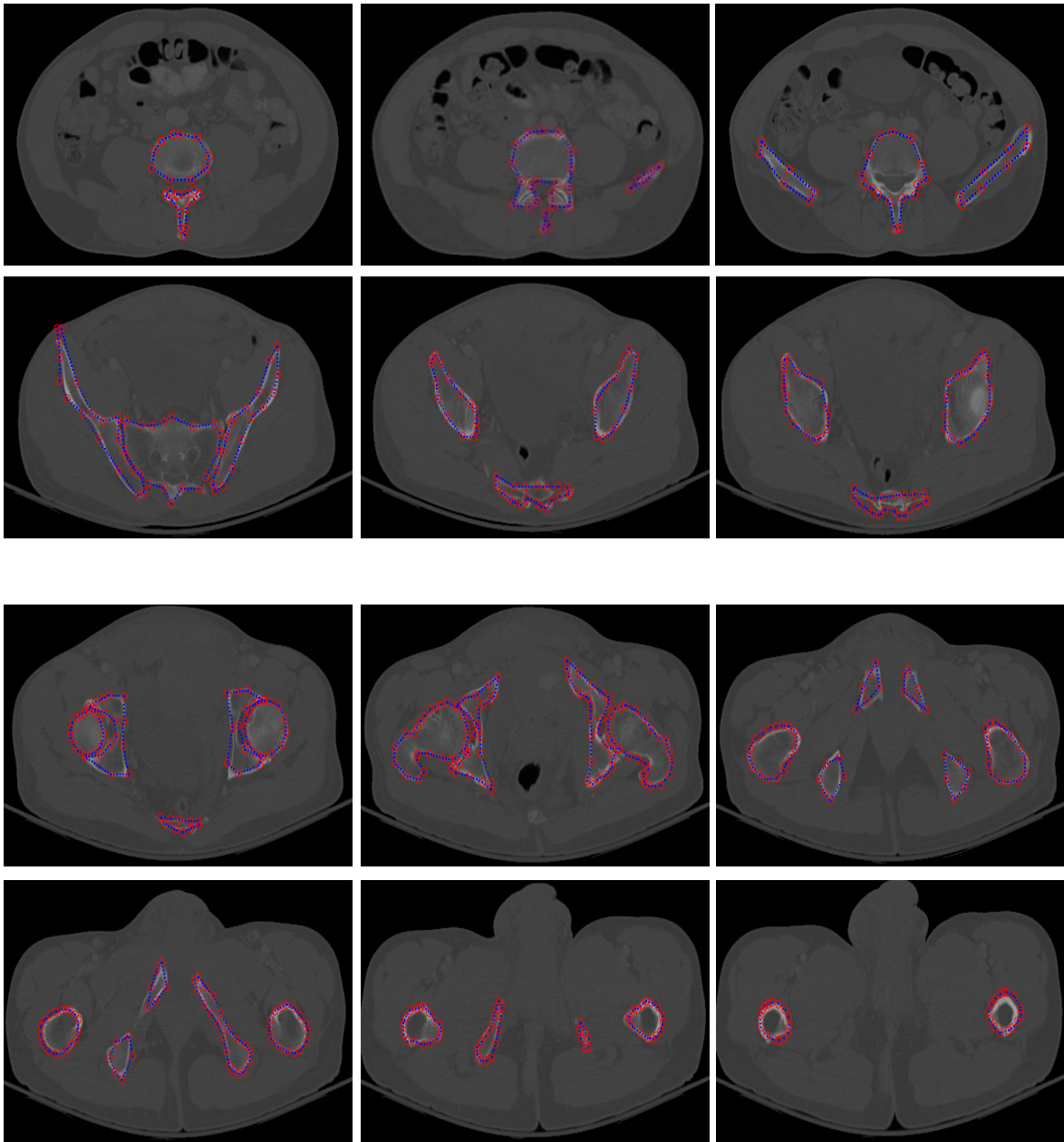


Figure 6.7: Example of pelvic bone segmentation results via RASM with automatic initialization.

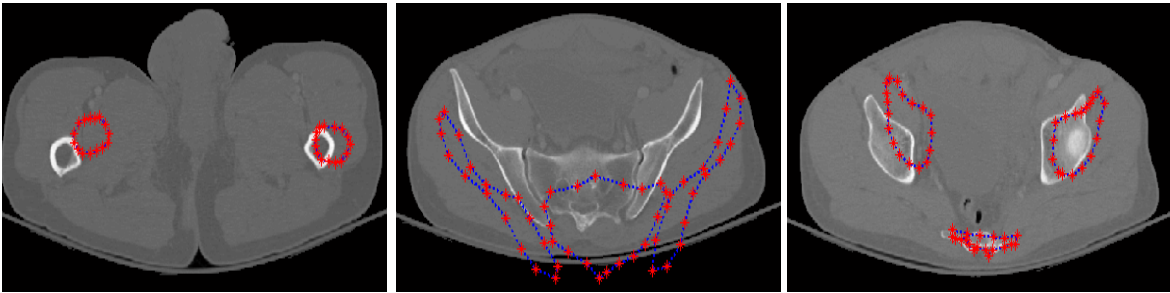


Figure 6.8: Example results of pelvic bone segmentation via Standard ASM without initialization.

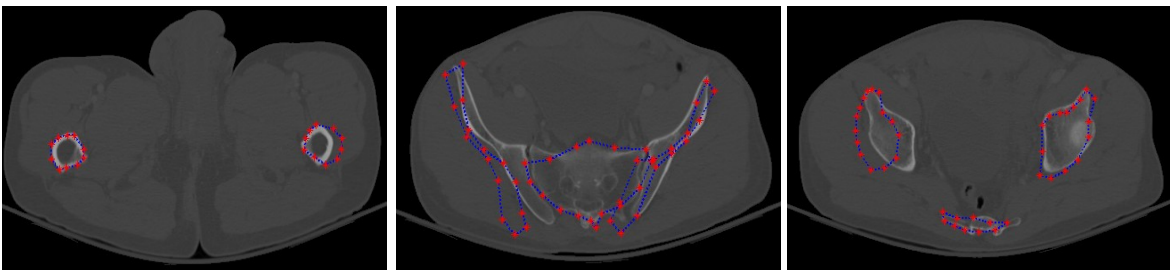


Figure 6.9: Example results of pelvic bone segmentation via Standard ASM with manual initialization.

Figure 6.10 shows an example of inaccurate segmentation results using the proposed method, this case occurs when the system lacks the shape model information to match the specific target bone structures. And for this specific case, the appearance of a small bone structure beside the sacrum is because the position of the patient is tilted when his CT scan is taken.

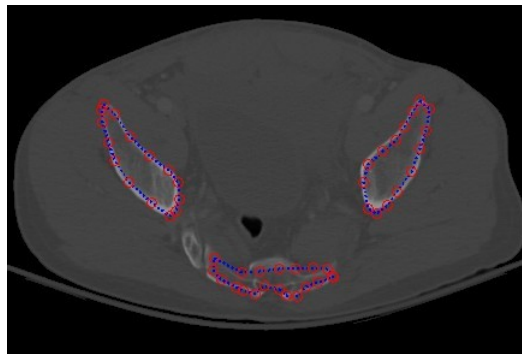


Figure 6.10 Inaccurate segmentation result.

6.3.7 Evaluation measures

In order to quantify the segmentation accuracy, suitable measure is required to evaluate the segmentation results. In this section we give precise definitions for evaluation criteria that we believe are useful and intuitive for evaluation purposes.

Mean Distance: Given two surfaces S_1 and S_2 we define the distance $d(p_n, S_2)$ between a point p_n on a surface S_1 and the surface S_2 as:

$$d(p_n, S_2) = \min_{p_m \in S_2} \|p_n - p_m\|_2 \quad (6.1)$$

We define the mean distance between surface S_1 and the surface S_2 as:

$$d(mean) = \frac{\sum_{n=1}^L d(p_n, S_2)}{L} \quad (6.2)$$

where $\|\cdot\|_2$ denotes the Euclidean norm, p_n denotes each landmark on surface S_1 and p_m denotes each landmark on surface S_2 , L denotes the total number of landmarks on the surface.

Mis-segmented Area: The idea is to have a measure that represents the uncommon area of the segmented surface and gold standard surface of pelvic bone. Given two surfaces S_1 and S_2 , we define the areas as A_1 and A_2 , the Mis-segmented Area MA of two surfaces S_1 and S_2 can be defined as:

$$\text{Cardinality}\{G\} \quad (6.3)$$

where:

$$G = \{pixels : p \mid p \in A_1 \cup A_2, p \notin A_1 \cap A_2\}$$

These results were evaluated by expert radiologist as ground truth for assessment. Visual inspection is also used for assisting to evaluate performance of pelvic bone

segmentation. The segmented bones are classified into three categories: Good, Acceptable, and Unacceptable. These categories were determined via consultation with a trauma physician, who identified actual bone contour as the ground truth.

The segmentation results can be represented with a mean distance, used to identify the segmentation result as one of these three classes. The shapes represented with mean distances of less than $1.6 \pm 0.2\text{mm}$ are classified as good, the shapes represented with mean distances between $1.6 \pm 0.2\text{mm}$ and $2.2 \pm 0.2\text{mm}$ are classified as acceptable, the shapes represented with mean distances more than $2.2 \pm 0.2\text{mm}$ are classified as unacceptable. The segmentation result can also be represented with a mis-segmented area, identifying the segmentation result as one of these three classes. The shapes represented with mis-segmented areas of less than 10% are classified as good, the shapes represented with mis-segmented areas between 10% and 20% are classified as acceptable, the shapes represented with mis-segmented areas more than 20% are classified as unacceptable. Among all the segmentation results of 886 testing images across fifteen patients, 83.07% of them are classified as good, and 13.54% of them are acceptable and 3.39% of them are detected to be unacceptable. The total segmentation accuracy for both good and acceptable classes is 96.61%.

For different pelvic bone structures, the segmentation accuracy results are shown in Figure 6.11. The ilium, ischium, pubis and femur are almost always detected to be at least acceptable; however, the sacrum and lumbar show a number of unacceptable results. This may be because of the variation in bone shapes, blurred edge of the bones, poor quality of the original image, etc. The unacceptable results may be improved by further training of

models across a wider dataset or using more landmarks for training the model. Segmentation accuracy, including both good and acceptable results of different pelvic bones using the proposed method, the Standard ASM with manual initialization and the Standard ASM without initialization, are shown in Figure 6.12. The results show the superiority of the proposed method on all types of pelvic bones.

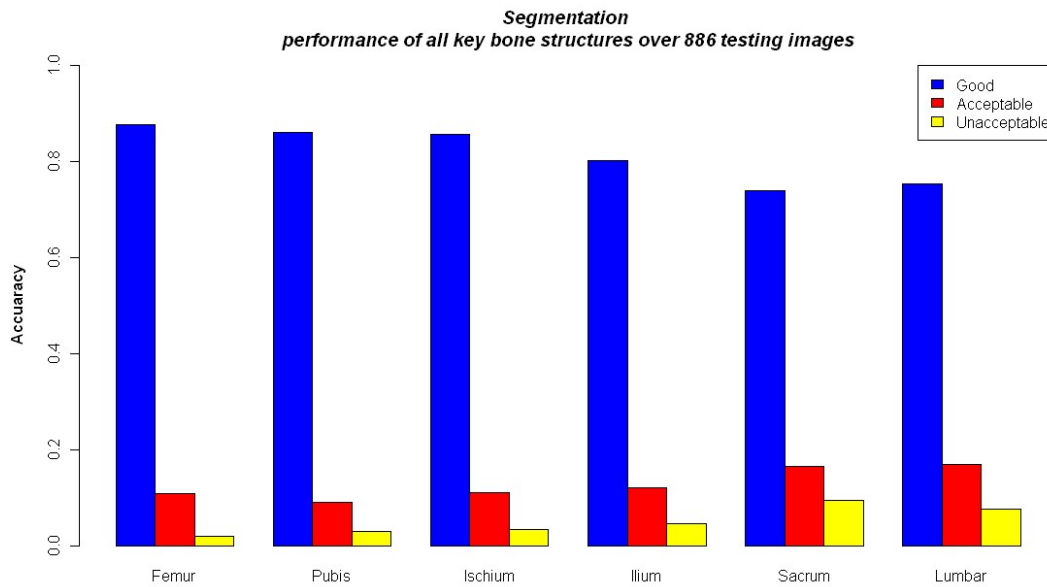


Figure 6.11 Segmentation accuracy results using proposed method of different pelvic bone structures.

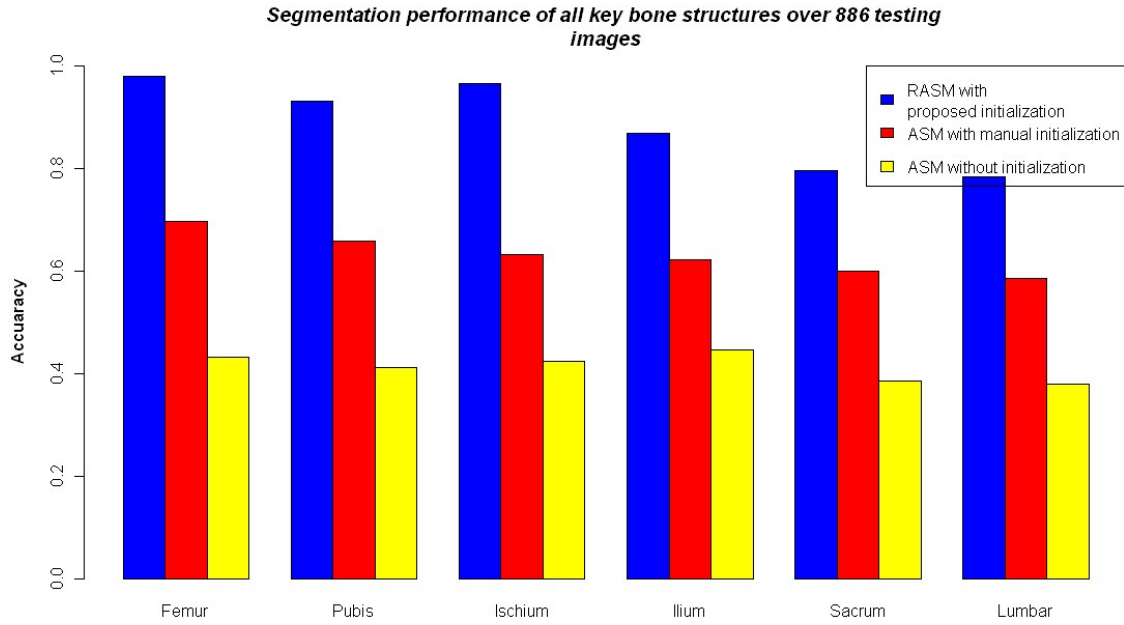


Figure 6.12 Segmentation accuracy including both Good and Acceptable results of different pelvic bones using proposed method, Standard ASM with manual initialization and Standard ASM without initialization.

6.3.8 Compared results with Snake

In this section we compare the segmentation performance using the proposed method and Active contour model (ACM), a special type of snakes. This method is often used in image segmentation. In Snakes, a deformable model is matched to a target in the image by means of energy minimization. A snake is initialized firstly near the target and the snake gets refined iteratively and moves towards the salient contour [80].

We compare the segmentation performance using our proposed method with the performance using an automated seeding based Snake method [81]. Selecting appropriate seeds is very important for obtaining a satisfied segmentation result. This paper presents a method of automatic initial seeds creation that is suitable for pelvic CT segmentation. Firstly initial bone mask is established using preprocessing, wavelet analysis and a suitable

threshold. Next, refined bone mask is obtained using binary multiplication of the initial bone mask and the filtered image after applying Gaussian filtering. In order to form seeds that are close to the contour, Canny edge detection is utilized based on the refined mask and seeds are most likely located on the edge of the identified regions of interest.

Seed growing step consists of growing each seed from the refined mask in its own neighborhood. The established growing criterion is based on neighborhood grey level statistics and gradient values. A curve is initialized based on the initial seeds. Such initial curve evolves and moves through the image according to a solution that attempts to minimize the energy function [81].

Figure 6.9 shows the compared results using the proposed method – RASM and the Snake method. The segmentation results using RASM are shown in the left side, the results using Snake in left side are shown in the right side. From the results, we can see that the snake method detect two separated bones as one object. There are often pelvic bone structures which may be close to each other, e.g. femoral head and ilium, such that snake method may fail to detect those close and separated bones. Also as can be seen in the third group results, the non-bone region is wrongly detected as bone structure using Snake.

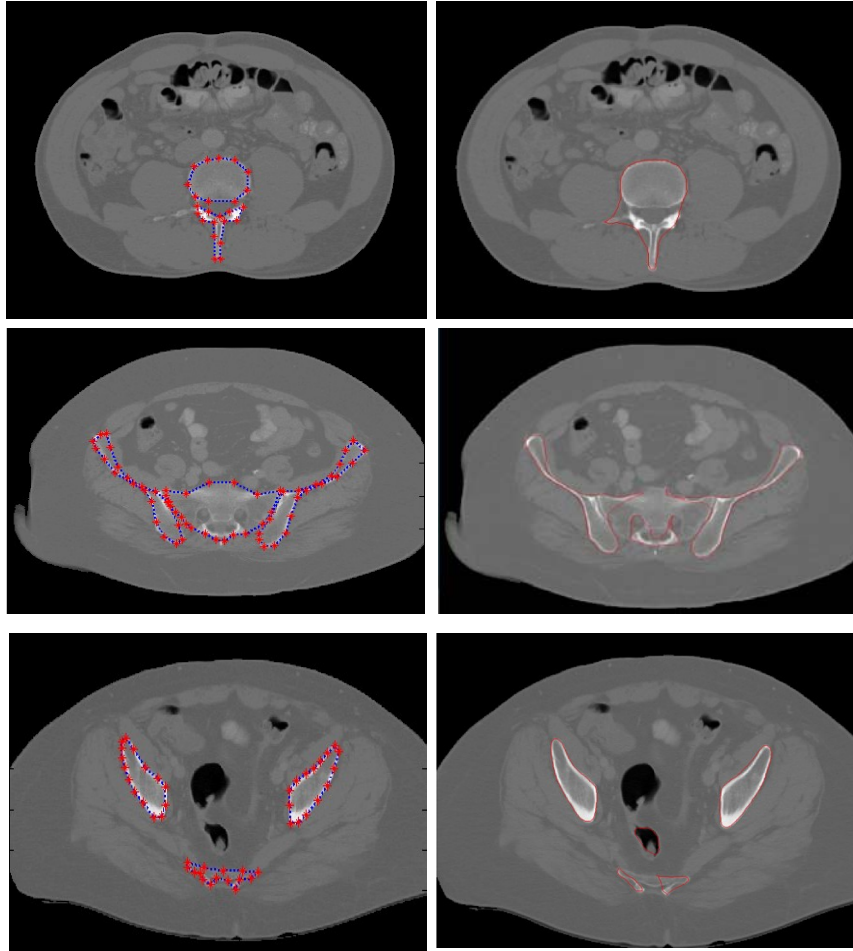


Figure 6.13: Compared results of pelvic bone segmentation via RASM and Snake methods.

6.3.9 Considerations during Training

Since ASM is a supervised learning method, we are required to test the reliability of the performance of training models. A cross-validation based method is designed to test how much different training data can affect the segmentation results.

For the entire dataset (twenty patients), we shuffle the order of these data sets. Then four folders of data are created based on twenty subjects, each folder has five

subjects, and we define the folders as A, B, C and D. Leave one folder out is utilized for the cross-validation process. One subject is selected each time from one folder for testing, the remaining subjects in other three folders are used for creating three different training models, which apply to each selected testing subject. This process is designed to avoid choosing overlapping data for creating different training models and make them independent with each other. Different key pelvic bone structures, including right ilium, left ilium, right femur, left femur, right pubis and left pubis are segmented to demonstrate and compare the performance of training models.

Table 6.2 shows the average segmentation performance for the testing subjects in A using three training models created from B, C, and D. Table 6.3 presents the average segmentation performance for the testing subjects in B using three training models created from A, C, and D. Table 6.4 shows the average segmentation performance for the testing subjects in C using three training models created from A, B, and D. Table 6.5 presents the average segmentation performance for the testing subjects in D using three training models created from A, B, and C. In the tables, MD denotes Mean Distance between the segmented surface and ground truth surface, which is defined in Chapter 6.3.7.

Figure 6.14 and Figure 6.15 show the example results of right pelvic ilium bone segmentation using three different training models for two testing subjects. Figure 6.16 and Figure 6.17 present the example results of left pelvic ilium bone segmentation using three different training models for two testing subjects. Figure 6.18 shows the example results of right pelvic femur bone segmentation using three different training models for a testing

subject. Figure 6.19 shows the example results of left pelvic femur bone segmentation using three different training models for a testing subject. Figure 6.20 shows the example results of right pelvic pubic bone segmentation using three different training models for a testing subject. Figure 6.21 shows the results of left pelvic pubic bone segmentation using three different training models for a testing subject.

For the segmentation performance, 90% of the total testing subjects are classified as good and there is slight difference among the segmentation results using different training models. Based on the entire performance of three different training models on key pelvic bone structures across testing subjects, we can conclude that the selection of training data to form training models has slight influence to the final segmentation results. Also, each training model performs well on different testing subjects and most of the segmentation results are classified as the Good. The created training models in this dissertation for pelvic bone segmentation are effective and reliable.

Table 6.2. Performance of three training models from B,C, and D for five testing subjects in A.

Testing Subjects/Training Model	Training Model B	Training Model C	Training Model D
First testing subject in A	Good MD: 0.6 ± 0.2 mm	Good MD: 1.0 ± 0.2 mm	Good MD: 1.5 ± 0.1 mm
Second testing subject in A	Good MD: 1.1 ± 0.2 mm	Good MD: 1.2 ± 0.3 mm	Good MD: 1.0 ± 0.2 mm
Third testing subject in A	Good MD: 0.8 ± 0.4 mm	Good MD: 1.0 ± 0.5 mm	Good MD: 0.9 ± 0.2 mm
Fourth testing subject in A	Acceptable MD: 1.7 ± 0.6 mm	Good MD: 1.5 ± 0.2 mm	Good MD: 1.3 ± 0.3 mm
Fifth testing subject in A	Good MD: 0.8 ± 0.2 mm	Good MD: 0.8 ± 0.2 mm	Good MD: 0.9 ± 0.4 mm

Table 6.3. Performance of three training models from A, C, and D for five testing subjects in B.

Testing Subjects/Training Model	Training Model A	Training Model C	Training Model D
First testing subject in B	Good MD: 1.5 ± 0.2 mm	Good MD: 1.6 ± 0.3 mm	Good MD: 1.3 ± 0.4 mm
Second testing subject in B	Good MD: 0.6 ± 0.2 mm	Good MD: 0.7 ± 0.4 mm	Acceptable MD: 2.2 ± 0.8 mm
Third testing subject in B	Good MD: 1.6 ± 0.3 mm	Good MD: 0.9 ± 0.2 mm	Good MD: 1.2 ± 0.2 mm
Fourth testing subject in B	Good MD: 1.6 ± 0.2 mm	Acceptable MD: 2.1 ± 0.7 mm	Good MD: 1.0 ± 0.2 mm
Fifth testing subject in B	Good MD: 1.1 ± 0.4 mm	Good MD: 0.8 ± 0.2 mm	Good MD: 1.0 ± 0.2 mm

Table 6.4. Performance of three training models from A, B, and D for five testing subjects in C.

Testing Subjects/Training Model	Training Model A	Training Model B	Training Model D
First testing subject in C	Good MD: 1.2 ± 0.4 mm	Good MD: 1.0 ± 0.2 mm	Good MD: 1.3 ± 0.3 mm
Second testing subject in C	Good MD: 0.8 ± 0.2 mm	Good MD: 0.6 ± 0.2 mm	Good MD: 0.6 ± 0.2 mm
Third testing subject in C	Acceptable MD: 2.2 ± 0.5 mm	Acceptable MD: 1.9 ± 0.3 mm	Good MD: 1.6 ± 0.3 mm
Fourth testing subject in C	Good MA: 1.6 ± 0.3 mm	Good MA: 1.5 ± 0.2 mm	Good MD: 1.3 ± 0.4 mm
Fifth testing subject in C	Good MD: 0.7 ± 0.2 mm	Good MD: 0.6 ± 0.2 mm	Good MD: 1.0 ± 0.1 mm

Table 6.5. Performance of three training models from A, B, and C for five testing subjects in D.

Testing Subjects/Training Model	Training Model A	Training Model B	Training Model C
First testing subject in D	Good MD: 1.1 ± 0.4 mm	Good MD: 1.1 ± 0.2 mm	Good MD: 1.2 ± 0.3 mm
Second testing subject in D	Good MD: 1.0 ± 0.2 mm	Good MD: 1.5 ± 0.2 mm	Good MD: 1.4 ± 0.4 mm
Third testing subject in D	Good MD: 0.8 ± 0.2 mm	Good MD: 1.3 ± 0.3 mm	Good MD: 0.9 ± 0.4 mm
Fourth testing subject in D	Good MD: 1.5 ± 0.4 mm	Good MD: 1.6 ± 0.2 mm	Acceptable MD: 2.1 ± 0.6 mm
Fifth testing subject in D	Good MD: 0.6 ± 0.2 mm	Good MD: 0.7 ± 0.3 mm	Good MD: 1.0 ± 0.3 mm

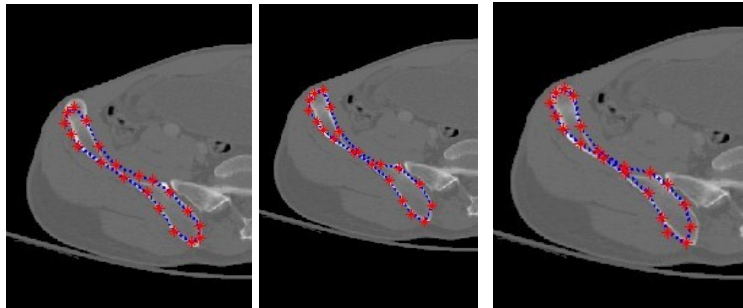


Figure 6.14: Results of pelvic ilium bone segmentation using three different training models for a testing subject.

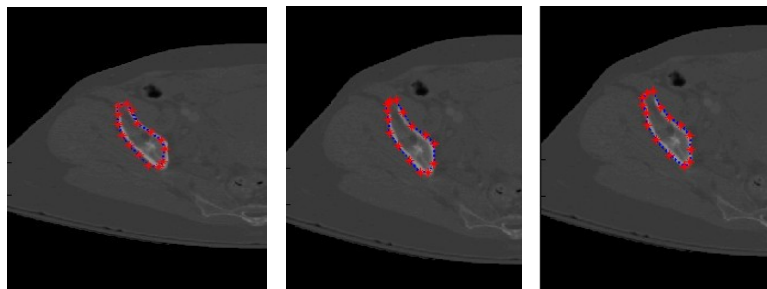


Figure 6.15: Results of pelvic ilium bone segmentation using three different training models for a testing subject.

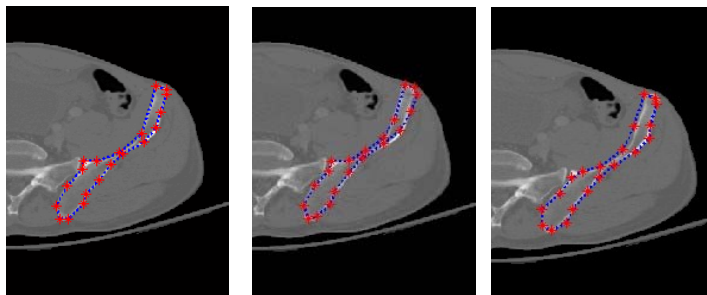


Figure 6.16: Results of pelvic ilium bone segmentation using three different training models for a testing subject.

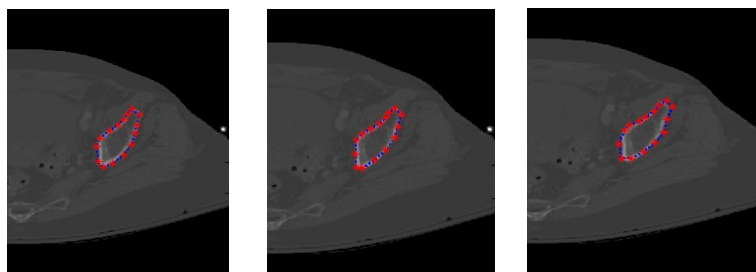


Figure 6.17: Results of pelvic ilium bone segmentation using three different training models for the second testing subject.

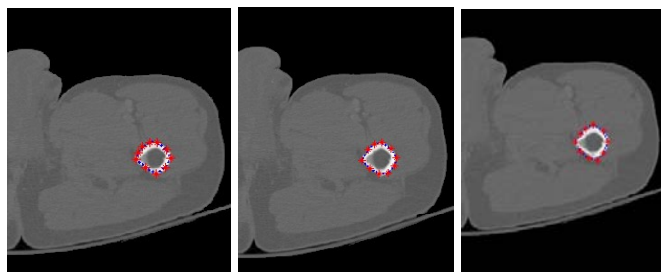


Figure 6.18: Results of pelvic femur bone segmentation using three different training models for a testing subject.

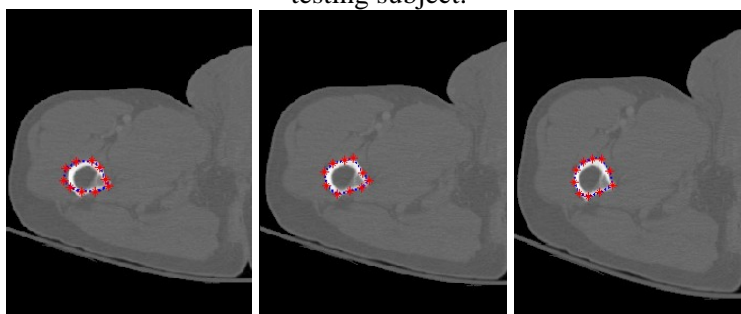


Figure 6.19: Results of pelvic femur bone segmentation using three different training models for a testing subject.

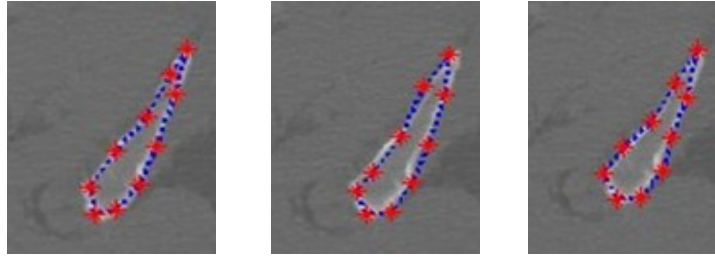


Figure 6.20: Results of pelvic pubic bone segmentation using three different training models for a testing subject.

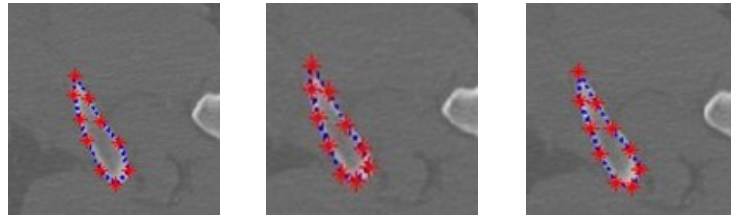


Figure 6.21: Results of pelvic pubic bone segmentation using three different training models for a testing subject.

6.4 Results for Fracture Detection

The results show that the method can successfully detect fracture even in the case of small fractures. Table 6.2 presents the performance of the method detecting fractures. The proposed method is highly sensitive to the discontinuities present in the bone and is also capable of detecting fractures that are very difficult to identify by visual inspection.

Figures 6.22 through 6.23 show the results obtained at various stages of fracture detection. In these Figures, (a) is the original image, (b) is the extracted adaptive window after being scaled, (c) is the enhanced window after brightness contrast enhancing. This is done for better visualization effect. In addition, Figure 6.22 (d) shows the final fracture detection results. In Figure 6.22, the patient suffers from a minor fracture in right iliac wing. Figure 6.22 (d) indicates the fracture detected in the right iliac wing. Figure 6.23 is the “no fracture” case. The result in Figure 6.23 (d) shows that the bone appears smooth

with no fracture. Figure 6.24 illustrates a patient with a very severe fracture in the right ilium bone. Fractures are detected from the windows of this bone region. Example of detected fractures shown in Figure 6.24 (d) indicates fractures in three different regions of the right ilium bone. These results are evaluated by an expert radiologist and are considered acceptable. For 8.5% of the cases, the method was unable to capture the fracture. This may be due to the blurred edge of the bones, and the poor quality of the original image.

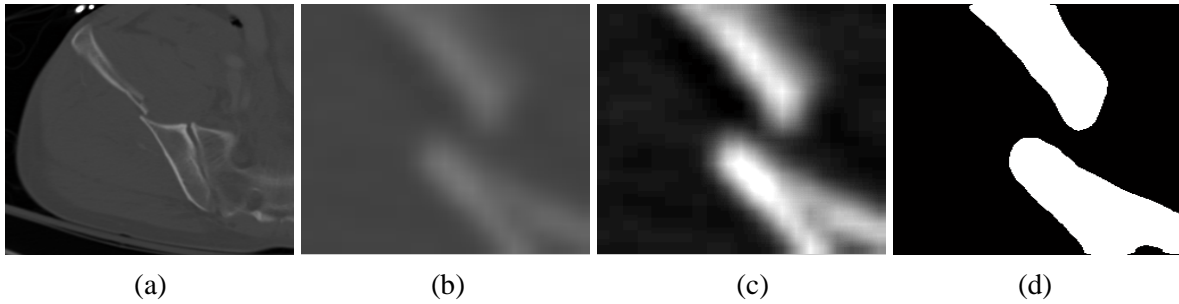


Figure 6.22. Example of a detected broken boundary of pelvic bone, which may indicate a fracture.

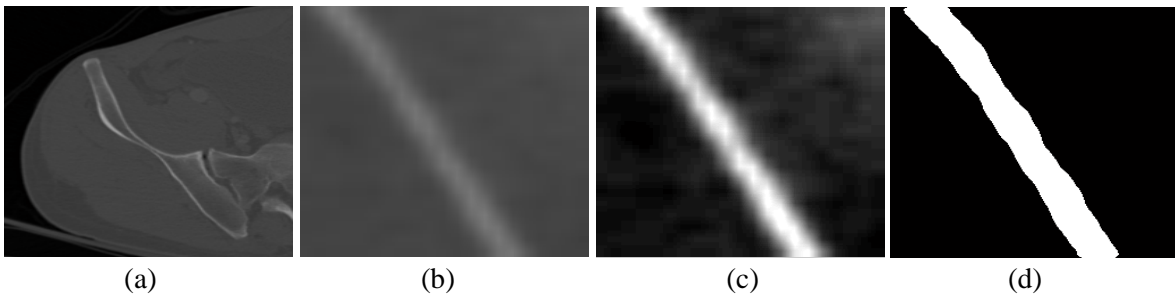


Figure 6.23: Example of a detected non-broken boundary of pelvic bone, which may indicate no fracture.

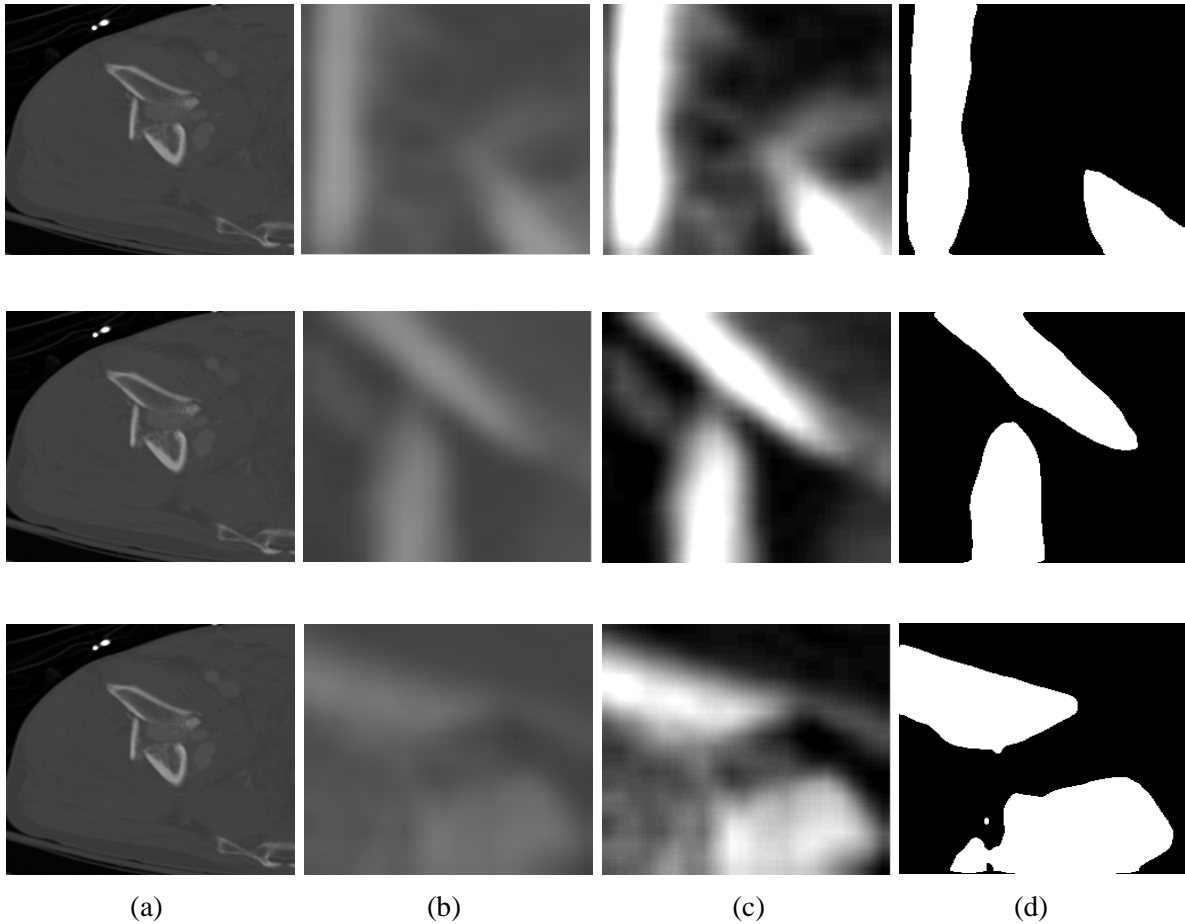


Figure 6.24: Example of a detected broken boundary of pelvic bone, which may indicate three fractures.

The results of the proposed method are evaluated using the following criteria:

sensitivity, specificity, and accuracy. We define the criteria as follows:

True positives: Fracture window correctly identified as fracture

False positives: Normal window incorrectly identified as fracture

True negative: Normal window correctly identified as normal

False negative: Fracture window incorrectly identified as normal

Sensitivity = $\frac{\text{number of true positives}}{\text{number of true positives} + \text{number of false negatives}}$

Specificity = $\frac{\text{number of true negative}}{\text{number of true negative} + \text{number of false positives}}$

Accuracy = (number of true positives + number of true negative)/ (number of true positives + false negatives+ true negative+ false positives)

All 1346 CT images of twenty patients are used to test the performance of the proposed method. 53880 adaptive windows are created based on all the landmarks. Table 6.6 presents the performance of the method detecting fractures. Relative high accuracy, sensitivity and specificity have been achieved, which show the validity and superiority of the proposed method for fracture detection.

Table 6.6. Performance of pelvic bone fracture detection.

Statistical Results	Accuracy	Sensitivity	Specificity
Rate %	89.5	91.5	89.5

Among all 53800 windows, 53200 windows have no fracture while 680 windows contain fractures. Since the number of non-fracture windows is much more than the windows with fractures. In order to avoid the existing unbalance of the data, we randomly select 700 non-fracture windows to make the entire dataset balanced and evaluate the performance of the proposed method. The results are presented in Table 6.7.

Table 6.7. Performance of pelvic bone fracture detection.

Statistical Results	Accuracy	Sensitivity	Specificity
Rate %	89.2	91.5	87

Most of the windows which include fractures are located in the Ilium bones. Approximately fifty percent of these bones contain two or more fractured sites. In clinical diagnosis, extra information can be provided to a physician examining these bone areas, including the blood vessels and nerves. This will allow the physician to see if there is any

associated injury. Nonsurgical treatment or surgical treatment plans can be decided based on the diagnosis decisions.

Figure 6.25 shows an inaccurate fracture detection result. This case happens because femoral head and ilium are too close to each other, such that part of both bones may fall into the same adaptive window. Thus, two broken bone pieces are detected in the window.

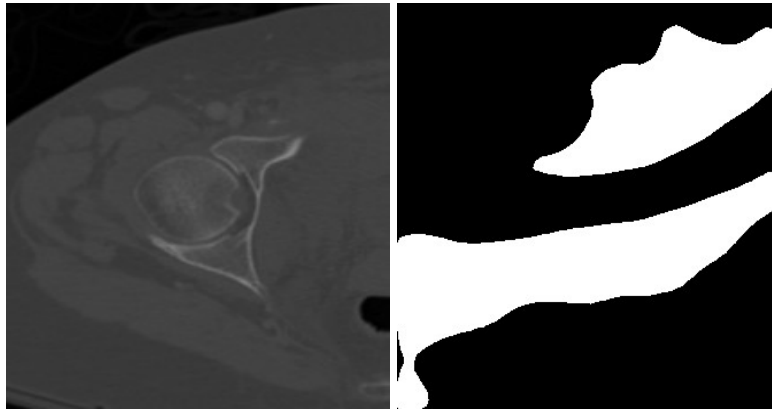


Figure 6.25: Example results of inaccurate fracture detection.

In order to address this issue, we design a method of comparing the inaccurate detected window to the best matching template to decide if the corresponding window contains fracture or not. After the best matching template is found, the bone structure is registered to the matched template using the method described in Chapter 4.3. Then, if any non-discontinuous window is detected, it is compared with the corresponding window at the same position in the best matching template to see if there is any discontinuity by the expert knowledge. If the expecting result in the template is non-fracture, then this is detected as a false-positive result. An example result is shown in Figure 6.26.

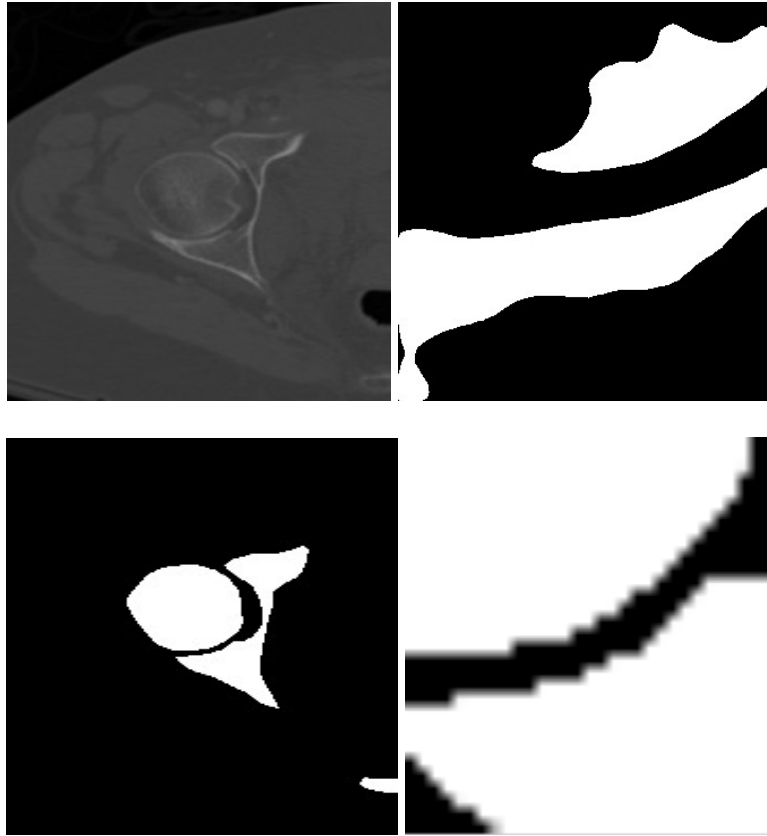


Figure 6.26: Example false-positive result.

The algorithm runs on MATLAB using a computer with a 2.80GHz Intel(R) Core(TM) i7 processor, 64-bit Operating System, and 6.0 GB memory. For each CT slice, it takes approximately 0.5 seconds more for the 2nd level of stationary wavelet decomposition than the first level of decomposition. The average runtime is thirty five seconds per slice. In C++, the average runtime reduces to five seconds per slice.

6.5 *Results of 3D pelvic bone structure modeling*

Since 2D pelvic CT images provide limited and local information in each slice, 3D pelvic bone models are very often required to present a full range of the entire bone structure in clinical diagnosis. The radiologists usually observe and analyze the patients'

data of both 2D slices and 3D bone models to make accurate diagnostic decisions. Figure 6.27 shows example results of 3D pelvic bone structure modeling. After the pelvic bone from each continuous 2D pelvic CT image is successfully segmented, the 3D model is reconstructed utilizing these extracted 2D bone structures. The models are created using the isosurface method, as described in chapter 4.6. As we can see from Figure 6.27, a human's 3D pelvic bone is clearly presented from different points of view. In our work, the pelvic model can be rotated to any angle which will help the physician comprehensively observe the entire pelvic bone structure and detect any abnormality of the patient. In addition, 3D visualization may be used for further validating the 2D segmentation results. However, for the specific measure of fracture or hemorrhage severity, 2D images should be utilized to provide more details. Figure 6.28 provides the 3D images of pelvic bones with fractures in Ilium bones.

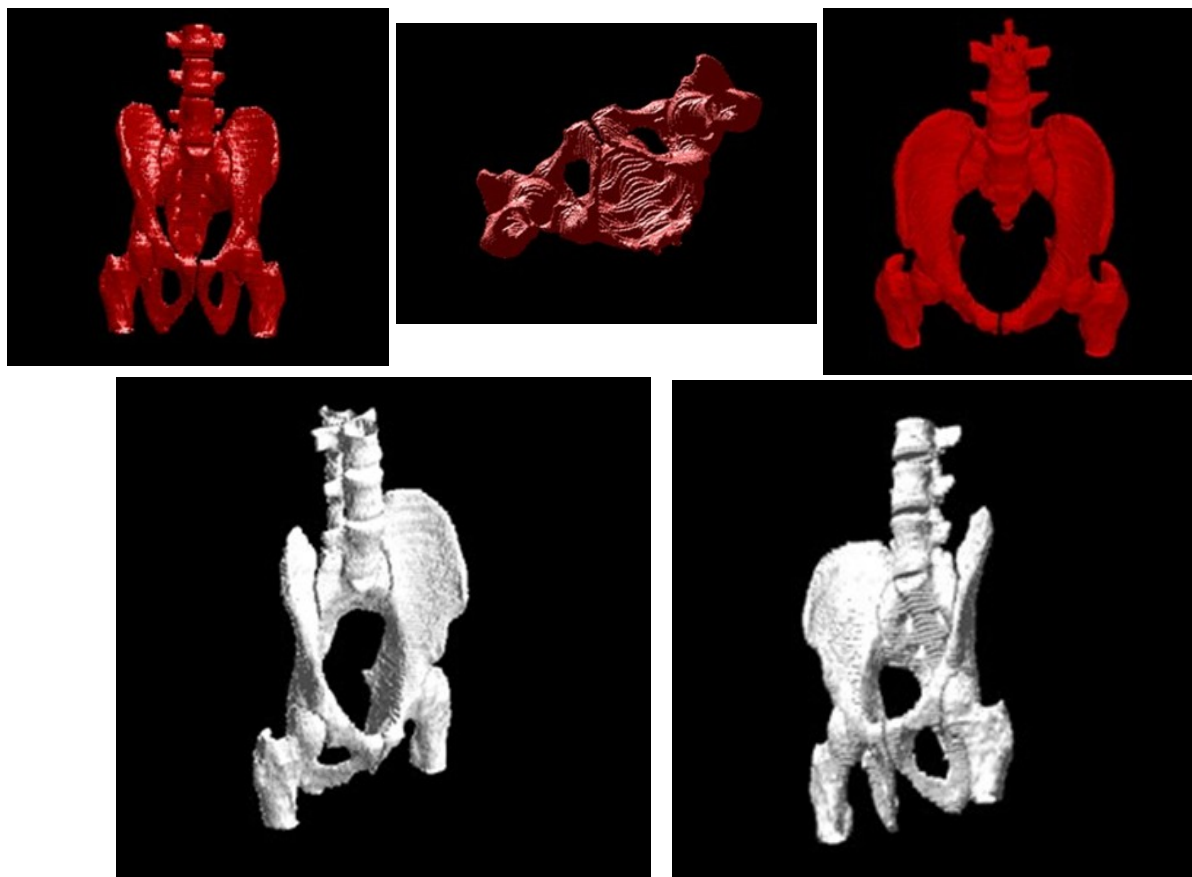


Figure 6.27: Example results of 3D pelvic bone structure.

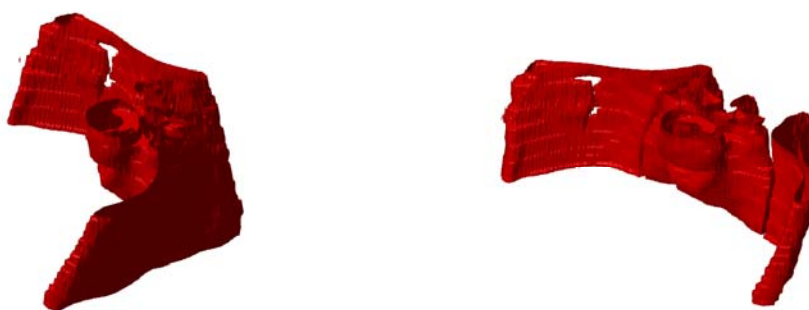


Figure 6.28: Example results of 3D pelvic bone structure with fractured Ilium bones.

6.6 *Summary and Discussion*

The main observations regarding the results based on the test images of the proposed methods are as follows:

- The designed steps using morphological operations form a successful method for eliminating the majority of surrounding artifacts and extracting the pelvic region.
- Brightness contrast stretching technique for image enhancement is involved in the proposed algorithm to emphasize the features of interest – the pelvic region, while simultaneously soft tissues and other organs are not the main focus of the analysis. This ensures that the original image quality is improved with much brighter regions of pelvic bones.
- Satisfying results have been achieved by performing the proposed edge detection methodology. This allows the detected edges to be matched with the best matching template. The steps include Canny edge detector, morphological operations to remove spurious edges, and sub-edges connection and elimination.
- Shape matching algorithm is applied to find the association between the detected edge of the examined slice and best matching template, which makes the entire segmentation automated. Results prove that using shape matching algorithm for detecting the best matching template obtain higher accuracy than 2D correlation coefficients.
- Homogeneity feature extraction provides a novel approach for feature extraction from original images for image registration. Visual evaluation shows that pelvic

bone regions are clearly defined yielding a relatively accurate representation of the bone tissue.

- A new image registration algorithm is formed using enhanced homogeneity feature extraction, correlation coefficient calculation for similarity measure, affine transformation, and Powell algorithm application. This image registration algorithm is combined with the ASM for developing the Registered Active Shape Model (RASM) algorithm to create a set of more robust training models which will result in better segmentation. Higher segmentation accuracy has been achieved using the RASM than the Standard ASM algorithm.
- Standard ASM is highly sensitive to initialization and requires an initial position to be correctly assigned to the training model in order to detect a target object in the image. Hence, an automated hierarchical initialization algorithm is used in the study. The proposed initialization process involves image registration, and bone feature extraction as well as edge detection to sequentially and automatically place the training models of each individual object for the test images to extract the bone from the background. Compared results demonstrate the proposed initialization process accurately place the shape models in the correct initial position of the bones. Created training models are also validated to be effective in extracting the pelvic bones. Compared results demonstrate that the proposed method can achieve better segmentation performance than the Snake method.

- After bone segmentation, 3D pelvic bone models are built based on all extracted bones from 2D images. All the slices are aligned with each other and the human pelvic bone structure is visually presented.
- Two evaluation measures – Mean Distance and Mis-segmented Area are defined to quantitatively evaluate the segmentation performance.
- After bone segmentation, a multi-stage process is used for fracture detection in pelvic CT scans. Fracture detection of pelvic bones includes several steps, they are adaptive window creation, 2-D SWT application, masking, boundary tracing. If there is a contour discontinuity in a window, then it is considered as a potential bone fracture. Visual enhancement and relative high accuracy, sensitivity and specificity show the superiority of the fracture detection algorithm.

CHAPTER 7 Conclusion and Future Work

7.1 Overview

This chapter provides a review of the main conclusions drawn from the methodologies and results described in this dissertation. Also, the chapter presents the future works which is the further exploration of the formation of the computer-assistant decision-making system for traumatic pelvic injuries.

7.2 Conclusions

This dissertation provides a framework for the pelvic bone segmentation and fracture detection. Pelvic CT scans of twenty patients are processed and bone structures from fifteen patients are accurately and automatically segmented using the proposed hierarchical approach which incorporates preprocessing, edge detection, Shape Matching, homogeneity based image registration and RASM with novel initialization. Segmentation results are evaluated using two quantitative measures and the compared results show that the proposed method performs better with higher segmentation accuracy than the Standard ASM. Also, compared results indicate that the proposed method performs better than Snake algorithm. Additionally, computation time taken by this method is less than the manual segmentation, making it practically applicable in automated processing of medical images. Different training models are created to segment key pelvic bone structures and the results show that the selection of training data does not have a large affect on the final segmentation performance. 3D pelvic bone models are built based on 2D segmentation results.

This dissertation also presents a method for detecting fractures in pelvic bones using adaptive windowing, boundary tracing, and 2-D Stationary Wavelet Transform while including anatomical information. The results show that the proposed method is capable of detecting even small fractures in pelvic bones. Automated fracture detection, once verified with more data, will be an invaluable component of a larger modular system to extract features from CT images for a computer-assisted decision-making system.

7.3 *Future Work*

Future work includes the following items:

- Process a larger database, with higher resolution CT images to improve the performance of the algorithm for segmenting the bones and detecting the bone fracture.
- Explore the quantitative measurement of fracture based on a larger dataset, e.g. horizontal displacement measure, as well as the determination of fracture type.
- Explore 3D bone segmentation algorithms based on pelvic CT images with higher resolution.
- Apply an appropriate rule-based methodology to generate rules for outcome prediction. This will form a decision-making system to provide Physicians with reliable recommendations on diagnosis as well as treatment planning.

7.4 *Summary*

In this chapter first the impact and the importance of the work was described. Then, the main conclusions of the proposed research were given. Finally, the main future work which needs to be conducted as the continuation of the project was outlined.

Bibliography

Bibliography

- [1] http://www.mercyhospital.org/content/greystone_689.htm
- [2] http://www.nigms.nih.gov/Education/Factsheet_Trauma.htm
- [3] <http://www.cdc.gov/niosh/injury/>
- [4] <http://www.yourlegalguide.com/workers-compensation-injuries/>
- [5] Y. JWR, B. AR, B. RJ. Pelvic fractures: value of plain radiography in early assessment and management. *Radiology*, pages160-445, 1986.
- [6] <http://www.trauma.org/index.php/main/article/668/>
- [7] S. Ali, T. Pedro, D. Joseph, O. Marcus, I. Kenji, M. R. Daniel, and D. Demetrios. Predictors of Positive Angiography in Pelvic Fractures: A Prospective Study, *Journal of the American College of Surgeons*, 207(5): 656-662, 2008.
- [8] M. A. Schiff, A. F. Tencer, and C. D. Mack. Risk factors for pelvic fractures in lateral impact motor vehicle crashes, *Accident Analysis & Prevention*, 40(1):387-391, 2008.
- [9] UMD. Ciren report: Consequences and costs of lower-extremity injuries, EMS University of Maryland National Study Center for Trauma, 2005.
- [10] Fracture of the Pelvis, <http://orthoinfo.aaos.org/topic.cfm?topic=a00223>
- [11] M. A. Png, Y. Chen, W. K. Leow, W. Hsu, and T. S. Howe. Computing neck-shaft angle of femur for x-ray fracture detection, *In Proc. Int. Conf. on Computer Analysis of Images and Patterns (LNCS 2756)*, Springer, 2003.
- [12] V. L. F. Lum, W. K. Leow, Y. Chen, T. S. Howe, and M. A. Png. Combining classifiers for bone fracture detection in x-ray images, *IEEE International Conference on Image Processing*, 2005.
- [13] Merriam-Webster Online Dictionary, <http://www.merriamwebster.com/dictionary/computed+tomography>, 2009.
- [14] <http://www.radiologyinfo.org/en/info.cfm?pg=bodyct>.
- [15] C. D. John, R. Arthur (1818). Cunningham's text-book of anatomy.
- [16] L. G. Shapiro and G. C. Stockman. *Computer Vision*, pages 279-325, 2001.

- [17] S.M. Larie and S.S. Abukmeil. Brain abnormality in schizophrenia: a systematic and quantitative review of volumetric magnetic resonance imaging studies, *J. Psych.*, 172:110–120, 1998.
- [18] P. Taylor. Invited review: computer aids for decision-making in diagnostic radiology— a literature review. *Brit. J. Radiol.*, 68:945–957, 1995.
- [19] A.P. Zijdenbos and B.M. Dawant. Brain segmentation and white matter lesion detection in MR images. *Critical Reviews in Biomedical Engineering*, 22:401–465, 1994.
- [20] A.J. Worth, N. Makris, V.S. Caviness, and D.N. Kennedy. Neuroanatomical segmentation in MRI: technological objectives. *Int. J. Patt. Rec. Art. Intel.*, 11:1161–1187, 1997.
- [21] V.S. Khoo, D.P. Dearnaley, D.J. Finnigan, A. Padhani, S.F. Tanner, and M.O. Leach. Magnetic resonance imaging (MRI): considerations and applications in radiotherapy treatment planning. *Radiother. Oncol.*, 42:1–15, 1997.
- [22] H.W. Muller-Gartner, J.M. Links, et al. Measurement of radiotracer concentration in brain gray matter using positron emission tomography: MRI-based correction for partial volume effects. *J. Cereb. Blood Flow Metab.*, 12:571–583, 1992.
- [23] N. Ayache, P. Cinquin, I. Cohen, L. Cohen, F. Leitner, and O. Monga. Segmentation of complex threedimensional medical objects: a challenge and a requirement for computer-assisted surgery planning and performance. *Computerintegrated surgery: technology and clinical applications*, pages 59–74, 1996.
- [24] W.E.L. Grimson, G.J. Ettinger, T. Kapur, M.E. Leventon, W.M. Wells, et al. Utilizing segmented MRI data in image-guided surgery. *Int. J. Patt. Rec. Art. Intel.*, 11:1367–1397, 1997.
- [25] C. Li; C. Kao; J.C. Gore; Z. Ding, Minimization of Region-Scalable Fitting Energy for Image Segmentation , *IEEE Transactions on Image Processing*, 17 (10) : 1940 – 1949 , 2008.
- [26] S. Vicente, V. Kolmogorov, C. Rother. Graph cut based image segmentation with connectivity priors, *IEEE Conference on Computer Vision and Pattern Recognition*, pages 1 – 8, 2008.
- [27] L. Ladický , C. Russell, P. Kohli, P. H.S. Torr. Associative hierarchical CRFs for object class image segmentation. *IEEE International Conference on Computer Vision*, pages 739 – 746, 2009.

- [28] G. Gerig, M. Jomier and M. Chakos. Valmet: A New Validation Tool for Assessing and Improving 3D Object Segmentation, *Medical Image Computing and Computer-Assisted Intervention – MICCAI 2001 Lecture Notes in Computer Science*, 2208: 516–523, 2001.
- [29] P.K. Sahoo, S. Soltani, and A.K.C.Wong. A survey of thresholding techniques. *Comput. Vis. Graph.Im. Proc.*, 41:233–260, 1988.
- [30] R.M. Haralick and L.G. Shapiro. Image segmentation techniques. *Comput. Vis. Graph. Im. Proc.*, 29:100–132, 1985.
- [31] G.B. Coleman and H.C. Andrews. Image segmentation by clustering. *Proc. IEEE*, 5:773–785, 1979.
- [32] J.C. Dunn. A fuzzy relative of the ISODATA process and its use in detecting compact well-sparated clusters. *Journal of Cybernetics*, 3:32–57, 1973.
- [33] T. Lei and W. Sewchand. Statistical approach to X-Ray CT imaging and its applications in image analysis – part II: A new stochastic model-based image segmentation technique for X-Ray CT image. *IEEE T. Med. Imag.*, 11(1):62–69, 1992.
- [34] Z. Liang, J.R. MacFall, and D.P. Harrington. Parameter estimation and tissue segmentation from multispectral MR images. *IEEE T. Med. Imag.*, 13:441–449, 1994.
- [35] J.C. Rajapakse, J.N. Giedd, and J.L. Rapoport. Statistical approach to segmentation of single-channel cerebral MR images. *IEEE T. Med. Imag.*, 16:176–186, 1997.
- [36] K. Held, E.R. Kops, B.J. Krause, W.M. Wells, R. Kikinis, et al. Markov random field segmentation of brain MR images. *IEEE T. Med. Imag.*, 16(6), 1997.
- [37] E. Gelenbe, Y. Feng, and K.R.R. Krishnan. Neural network methods for volumetric magnetic resonance imaging of the human brain. *Proc. IEEE*, 84:1488–1496, 1996.
- [38] L.O. Hall, A.M. Bensaid, L.P. Clarke, R.P. Velthuisen, M.S. Silbiger, and J.C. Bezdek. A comparison of neural network and fuzzy clustering techniques in segmenting magnetic resonance images of the brain. *IEEE T. Neural Networks*, 3:672–682, 1992.
- [39] Z. Peter, V. Bousson, C. Bergot, and F. Peyrin. A constrained region growing approach based on watershed for the segmentation of low contrast structures in bone micro-ct images, *Pattern Recognition*, 41(7), 2008.

- [40] J. Yao, M. Miller, M. Franaszek, and R.M. Summers. Colonic polyp segmentations in ct colonography-based on fuzzy clustering and deformable models, *IEEE Transactions on Medical Imaging*, 23(11):1344-1352, November 2004.
- [41] T. McInerney and D. Terzopoulos. Deformable models in medical image analysis: a survey. *Medical Image Analysis*, volume 1: 91–108, 1996.
- [42] J.B.A. Maintz and M.A. Viergever. A survey of medical image registration. *Medical Image Analysis*, volume 2:1–36,1998.
- [43] S.D. Pathak, P.D. Grimm, V. Chalana, and Y. Kim. Pubic arch detection in transrectal ultrasound guided prostate cancer therapy. *IEEE Transaction on Medical Imaging*, 17(5):762–771, 1998.
- [44] L. Vincent and P. Soille. Watersheds in digital spaces: an efficient algorithm based on immersion simulation. *IEEE Transaction on Pattern Analysis and Machine Intelligence*, 13(6):583–598, 1991.
- [45] L. I Kuncheva and L. C Jain. Nearest neighbor classifier: Simultaneous editing and feature selection, *Pattern Recognition Letters*, 20(11–13): 1149–1156, November 1999.
- [46] T. Denoeux. A k-nearest neighbor classification rule based on Dempster-Shafer theory. *IEEE Transactions on Systems, Man and Cybernetics*, 25(5): 804 - 813, 1995.
- [47] J. Aldrich. R.A. Fisher and the making of maximum likelihood 1912–1922. *Statistical Science*, 12 (3): 162–176, 1997.
- [48] S.Y. Ji, R. Smith, T. Huynh, and K. Najarian. A comparative analysis of multi-level computer-assisted decision making systems for traumatic injuries. *BMC Medical Informatics and Decision Making*, 9(2), 2009.
- [49] L. Jong-Sen. Digital Image Enhancement and Noise Filtering by Use of Local Statistics *IEEE Transactions on Pattern Analysis and Machine Intelligence*, PAMI-2(2): 165 – 168, March 1980.
- [50] K. Najarian, R. Splinter. *Biomedical signal and image processing*, pages 41-43, 2006.
- [51] J. Canny, A Computational Approach To Edge Detection, *IEEE Trans. Pattern Analysis and Machine Intelligence*, 8(6):679–698, 1986.
- [52] M.Hagedoorn, Pattern Matching Using Similarity Measures, PhD thesis, Universiteit Utrecht, 2000.

- [53] R.C. Veltkamp and M.Hagedoorn, State of the Art in Shape Matching, *Technical Report UU-CS-1999-27*, Utrecht, 1999.
- [54] E.Persoon and K.Fu. Shape Discrimination Using Fourier Descriptors. *IEEE Trans. Systems, Man and Cybernetics*, 7(3):170-179, Mar. 1977.
- [55] C.Zahn and R.Roskies, Fourier Descriptors for Plane Closed Curves, *IEEE Trans. Computers*, 21(3): 269-281, Mar.1972.
- [56] T. B. Sebastian, P. N. Klein, and B. B. Kimia. Recognition of shapes by editing their shock graphs. *IEEE Transaction on Pattern Analysis and Matching Intelligence*, 26(5):550– 571, May 2004.
- [57] D. Sharvit, J. Chan, H. Tek, and B. Kimia. Symmetry-based indexing of image databases. *J. Visual Comm. and Image Representation*, 9(4):366–380, Dec. 1998.
- [58] D.Huttenlocher, G.Klanderman, and W.Rucklidge, Comparing Images Using the Hausdorff Distance. *IEEE Trans. Pattern Analysis and Machine Intelligence*, 15(9):850-863, Sept.1993.
- [59] A. Peter, A. Rangarajan, and J. Ho. Shape l'A^ne rouge: Sliding wavelets for indexing and retrieval. *IEEE Conf. Computer Vision and Pattern Recognition*, pages 1–8, 2008.
- [60] M. Oren, Constantine Papageorgiou, Pawan Sinha, Edgar Osuna, and Tomaso Poggio. Pedestrian detection using wavelet templates. *Computer Vision and Pattern Recognition*, pages 193–199, 1997.
- [61] S. Belongie, J. Malik, and J. Puzicha. Shape matching and object recognition using shape contexts. *IEEE Trans. Pattern Anal. Mach. Intell.*, 24(4):509–522, 2002.
- [62]D.H. Cooper, T.F. Cootes, C.J. Taylor, and J. Graham. Active shape models – their training and application. *Computer Vision and Image Understanding*, pages 38–59, 1995.
- [63] M. Oren, C. Papageorgiou, P. Sinha, E. Osuna, and T. Poggio. Pedestrian detection using wavelet templates. *Proc. Computer Vision and Pattern Recognition*, pages 193–199, 1997.
- [64] http://www.nlm.nih.gov/research/visible/visible_human.html
- [65] H. Cheng, and Y. Sun. A Hierarchical Approach to Color Image Segmentation Using Homogeneity. *IEEE Transactions on image processing*, 9(12): 2071 - 2082, 2000.

- [66] F. Maes, D. Vandermeulen, and P. Suetens, Comparative evaluation of multiresolution optimization strategies for multimodality image registration by maximization of mutual information, *Medical image analysis*, 3(4): 373-386, 1999.
- [67]http://www.pcmag.com/encyclopedia_term/0,2542,t=bilinear+interpolation&i=38607,00.asp
- [68]G. P. Nason, B. W. Silverman, *The stationary wavelet transform and some statistical applications*, *Lecture Notes in Statistics*, volume 103: 281-299, 1995.
- [69]N. Otsu, “A threshold selection method from gray level histograms,” *IEEE Trans. Systems, Man and Cybernetics*, volume 9: 62–66, March 1979.
- [70] L. G. Brown, A survey of image registration techniques, ACM Computing Surveys (CSUR) archive, 24 (4): 325 - 376, December 1992.
- [71]M. H. Moghari and P. Abolmaesumi, Global Registration of Multiple Bone Fragments using Statistical Atlas Models: Feasibility Experiments, 30th Annual IEEE International Conference of the Engineering in Medicine and Biology Society, pp.5374 – 5377, 2008.
- [72]M. H. Moghari and P. Abolmaesumi, “Global Registration of Multiple Point Sets: Feasibility and Applications in Multi-fragment Fracture Fixation”, Proceedings of MICCAI (2), pp.943-950, 2007.
- [73]S. Winkelbach, R. Westphal, and T. Gösling, “Pose Estimation of Cylindrical Fragments for Semi-automatic Bone Fracture Reduction”, in Proc. DAGM-Symposium, pp.566-573, 2003.
- [74]Douglas TS, Sanders V, Pitcher R, van As AB. “Early detection of fractures with low-dose digital x-ray images in a pediatric trauma unit”, *Journal of Trauma Injury, Infection, and Critical Care*, 65(1):E4-7, 2008.
- [75]M. A. Png, Y. Chen, W. K. Leow, W. Hsu, and T. S. Howe, “Computing neck-shaft angle of femur for x-ray fracture detection,” *In Proc. Int. Conf. on Computer Analysis of Images and Patterns (LNCS 2756)*, pp. 82–89, Springer, 2003.
- [76]V. L. F. Lum, W. K. Leow, Y. Chen, T. S. Howe, and M. A. Png, “Combining classifiers for bone fracture detection in x-ray images,” *IEEE International Conference on Image Processing*, vol. 1, pp. I–1149–52, Sept. 2005.
- [77] J. Wu, P. Davuluri, K. Ward, C. Cockrell, R. Hobson, K. Najarian, A New Hierarchical Method for Multi-level Segmentation of Bone in Pelvic CT Scans, *IEEE*

Engineering in Medicine and Biology Society (EMBC '11, oral), Boston, U.S.A, 2011, pp.3399-3402

[78] J. Wu, P. Davuluri, K. Ward, C. Cockrell, R. Hobson, K.Najarian, Fracture detection in traumatic pelvic CT images, *International Journal of Biomedical Imaging*, Volume 2012, Article ID 327198, pp. 1-10.

[79] J. Wu, P. Davuluri, A. Belle, C. Cockrell, Y. Tang, K. Ward, K.Najarian, R. Hobson, Fracture detection and quantitative measure of displacement in pelvic CT images, *Proceedings of 2011 International Workshop on Biomedical and Health Informatics, part of IEEE International Conference Bioinformatics & Biomedicine*, Atlanta, GA, 2011, pp.600-606.

[80] M. Kass, A. Witkin, and D. Terzopoulos, Snakes: Active Contour Models, *International Journal of Computer Vision*, 321-331 (1988).

[81] S.Vasilache , K.Najarian, A unified method based on wavelet filtering and Active Contour Models for segmentation of Pelvic CT images , *ICME International Conference on Complex Medical Engineering*, 2009.